

ALMA MATER STUDIORUM
UNIVERSITÀ DI BOLOGNA

SCHOOL OF ENGINEERING AND ARCHITECTURE
Forlì Campus

SECOND CYCLE MASTER'S DEGREE IN
INGEGNERIA AEROSPAZIALE/AEROSPACE ENGINEERING
Class LM-20

GRADUATION THESIS
in Radio Communication and Radar Systems

Design and Implementation of a
Non-Destructive Defect Detection Technique
Based on UWB-SAR Imaging

CANDIDATE
IGOR GAI

SUPERVISOR
Prof. ENRICO PAOLINI

CO-SUPERVISORS
Prof. ENRICO TROIANI
Prof. ANDREA GIORGETTI

Academic Year 2015-2016

To my FAMILY and my FRIENDS.

Abstract

In the last twenty years aerospace and automotive industries started working widely with composite materials, which are not easy to test using classic Non-Destructive Inspection (NDI) techniques. Pairwise, the development of safety regulations sets higher and higher standards for the qualification and certification of those materials.

In this thesis a new concept of a Non-Destructive defect detection technique is proposed, based on Ultra Wide-Band (UWB) Synthetic Aperture Radar (SAR) imaging. Similar SAR methods are yet applied either in mine-field [22] and head stroke [14] detection. Moreover feasibility studies have already demonstrated the validity of defect detection by means of UWB radars [12, 13].

The system was designed using a cheap commercial off-the-shelf radar device by Novelda and several tests of the developed system have been performed both on metallic specimen (aluminum plate) and on composite coupon (carbon fiber).

The obtained results confirm the feasibility of the method and highlight the good performance of the developed system considered the radar resolution. In particular, the system is capable of discerning healthy coupons from damaged ones, and correctly reconstruct the reflectivity image of the tested defects, namely a 8×8 mm square bulge and a 5 mm drilled holes on metal specimen and a 5 mm drilled hole on composite coupon.

Acronyms

AC	Alternating Current
c.d.f.	Cumulative Density Function
CG	Crack Growth
CT	Computed Tomography
DAA	Detect and Avoid
DC	Direct Current
DMS	Distance Measurement System
EIRP	Equivalent Isotropically Radiated Power
EM	Electromagnetic
FCC	Federal Communications Commission
FFT	Fast Fourier Transform
EU	European Union
I/O	Input / Output
iFFT	inverse Fast Fourier Transform
IEEE	Institute of Electrical and Electronics Engineers
IR	Infrared

LDC	Low Duty Cycle
LHS	Left Hand Side
LTI	Linear and Time Invariant
MaSTeR Lab	Material Structure Technology Research Laboratory
MF	Matched Filter
NDI	Non-Destructive Inspection
PAM	Pulse Amplitude Modulator
p.d.f.	Probability Density Function
POI	Point of Interest
POV	Point of View
RADAR	Radio Detection and Ranging
RCS	Radar Cross Section
RF	Radio Frequency
RHS	Right Hand Side
ROI	Region of Interest
RS	Residual Strength
SAR	Synthetic Aperture Radar
SNR	Signal to Noise Ratio
ToA	Time of Arrival
UV	Ultraviolet
US	United States
UWB	Ultra Wide-Band

Contents

Abstract	i
Acronyms	iii
Introductions	xv
1 NonDestructive Testing	1
1.1 Non-Destructive Testing outlines	1
1.2 Non-Destructive Testing classification	2
1.2.1 Optical methods	3
1.2.2 Liquid penetrant	5
1.2.3 Magnetic-particles	7
1.2.4 Eddy current	8
1.2.5 Radiography	10
1.2.6 Ultrasound	12
1.2.7 Thermography	15
1.3 Summary	17
2 Radar technology	21
2.1 Introduction	21
2.2 Narrow-band radar	21
2.3 UWB radars	25
2.3.1 UWB regulation	26
2.4 Novelda NVA6201 radar overview	30

2.4.1	Antennas	32
2.5	Synthetic Aperture Radar	32
2.5.1	Scanning process	32
2.5.2	Resolution	34
2.5.3	Processing	35
2.5.4	Image properties	35
3	System development	37
3.1	SAR application	37
3.2	Setup	38
3.3	Acquisition	39
3.4	Preliminary data processing	40
3.4.1	Resampling	41
3.4.2	Pulse convolution (Matched filtering)	42
3.4.3	Realignment	44
3.5	Image formation	45
3.5.1	Introduction	46
3.5.2	Imaging algorithm	50
3.5.3	Geometric considerations	51
3.5.4	Weight matrix	56
3.6	Defect detection	57
3.6.1	Plate scanning	58
3.6.2	Data processing	58
3.6.3	Database comparison	59
3.7	Summary	61
4	Experimental results	63
4.1	Test campaign	63
4.2	Considerations	63
4.2.1	Distance focusing	65
4.2.2	Gaussian weighting tradeoff	66
4.2.3	General issues	70

4.3	Database samples	70
4.3.1	Metal plate	71
4.3.2	Composite plate	76
4.4	Specimens	80
4.4.1	Metal plate	81
4.4.2	Composite plate	87
5	Conclusions	91
	Conclusions	91
5.1	Shortcomings	91
5.1.1	Method overview	91
5.2	Future developments	94
	Bibliography	99

List of Figures

1.1	Optical technique	4
1.2	Red and fluorescent dye comparison	5
1.3	Liquid penetrant technique procedure	6
1.4	Magnetic-particle physical principle	7
1.5	Magnetic-particle testing	8
1.6	Eddy current physical principle	9
1.7	Radiography principle	11
1.8	Computed Tomography example	12
1.9	Echo technique	13
1.10	Thermal Imaging of a wing	16
2.1	Radar block diagram	22
2.2	The Novelda radar NVA6201 with antenna lens	30
2.3	Novelda NVA6201 generated radar pulse	31
2.4	Antenna radiation pattern (with lens)	33
2.5	Side looking radar imaging geometry	34
2.6	ESA ERS-2 image of Rome	36
3.1	Cable dimension scheme	38
3.2	SAR scan pattern and waveform storage	39
3.3	Typical acquired waveform	40
3.4	Example of FFT resampled signal	41
3.5	Waveform after filtering	43
3.6	Matched filter behavior	44

3.7	Kroneker delta pulse	46
3.8	Radar - plate configuration	47
3.9	Radar generic configuration	47
3.10	Defect location based on two observations	48
3.11	Convex bulge problem	49
3.12	Concave bulge problem	49
3.13	SAR imaging areas	52
3.14	SAR: 2D geometric problem	53
3.15	SAR: 3D geometric problem	54
3.16	Weight matrix	57
3.17	Sliding window for corr2 computation	60
3.18	Process flowchart	62
4.1	Effects of reference plane shifting	67
4.2	Specimen M2 reconstructed images at different Gaussian vari- ance	69
4.3	Metal plate draw	71
4.4	Metal healthy plate	72
4.5	Metal healthy plate reconstructed image	72
4.6	Metal plate with central bulge	73
4.7	Metal plate with central bulge reconstructed image	74
4.8	Metal plate with central hole	75
4.9	Metal plate with central hole reconstructed image	76
4.10	Composite healthy plate reconstructed image	77
4.11	Composite plate with central hole	78
4.12	Composite plate with central hole reconstructed image	79
4.13	Composite plate with central hole cropped samples	80
4.14	Specimen M1 reconstructed image	81
4.15	Specimen M1 correlation maps	82
4.16	Specimen M1 template positioning	83
4.17	Specimen M1 correlation maxima	84
4.18	Specimen M1 correlation maxima position	85

4.19 Specimen M2 reconstructed image	86
4.20 Specimen M2 correlation maxima	87
4.21 Specimen C1 reconstructed image	88
4.22 Specimen C1 correlation maxima	89
5.1 Phased array antenna working principle	97

List of Tables

1.1	NDI summary	19
1.2	NDI summary (cont.)	20
2.1	Generic UWB usage power restriction (2014/702/EU).	29
2.2	Novelda radar settings	31
4.1	Specimen M1 - templates correlation peaks	83
4.2	Specimen M2 - templates correlation peaks	86
4.3	Specimen C1 - templates correlation peaks	88
5.1	UWB-SAR NDI summary	94

Introduction

This thesis work was carried out at the Telecommunication laboratory of the School of Engineering and Architecture in Cesena. Both the theory background and the practical realization of the design are herein presented before the results are shown. This essay is structured as follows:

Chapter 1 contains a brief overview of the most commonly used methods available for NDIs.

Chapter 2 presents the principle of work of radar devices, classic and UWB ones. It also introduces the description of Novelda NVA6201 device used to develop the system, and concludes with a SAR outline.

Chapter 3 addresses the design and development of the UWB-SAR object of this thesis.

Chapter 4 is a report of the obtained results, including data and comments.

Chapter 5 finally contains the shortcomings about the developed system and a critical view of the results achieved to propose future developments.

Chapter 1

NonDestructive Testing

1.1 Non-Destructive Testing outlines

NDI is a wide group of testing methods applied in material science and constructions. Their primary aim is to detect defects of the material, with an accuracy dependent on the applied principle. Some of the NDIs are also able to compute the position and shape of the defect and eventually provide its 3D reconstruction. These kind of testing methods are commonly used in a large variety of engineering fields, among which we found aerospace and civil ones, but also forensics as well as medicine.

Birth and enhancement of NDI is almost pairwise with the evolution of aerospace industry, since accurate inspection and evaluation of damages give an higher reliability and let use lower safety factors, such that lighter structures could be designed. Simultaneously, the update of safety regulations provided - in aeronautics - by CS 25, requires specific test to be performed on structures at each step of the tailoring process, from the raw material acceptance to the inspection of the component before the assembly and during the operative life. In this sense, NDIs represent a fundamental mean to demonstrate the reliability of the structures. Design philosophy evolved from Safe-Life, i.e. finite life, through Fail-Safe, which relies on redundant elements, to Damage Tolerance, i.e. the capability of withstand design load

in presence of damages. This latter one requires the evaluation of the time interval during which the component is statistically un-probable to broke. If the component is metallic, this step takes into account the concept of Crack Growth (CG), which uses the physical and mechanical properties of the material and the expected load spectrum to compute the damage evolution and the Residual Strength (RS). Once computed this time window, the inspection interval is set such to schedule at least some test in the observation window. Thus damages could be detected and the component substituted before the failure.

The employment of NDIs is an essential requirements for the state-of-the-art industries, to provide competitive and safe products. As we move to aerospace industry, NDIs are required for elements, components and structure to demonstrate the freedom from flaws, damages or any other undesired defect that could affect the product, as well as a mean to monitor its in-service usage.

1.2 Non-Destructive Testing classification

NDIs could be catalogued depending on power requirement or physical principles employed. A first distinction could be done between active and passive NDIs. The former requires some kind of energy - electric, magnetic or thermal. In case a defect is present, a macroscopic variation of the input energy is detected. Many techniques such as ultrasonic, tomography or active thermography belong to this group. On the other hand passive methods are simply based on observation of the specimen without introducing any kind of energy. Liquid penetrant, magnetic-particles and optic methods belong to passive NDIs.

Another distinction is based upon the ability of deep flaws detection. Surface, sub-surface or volumetric techniques depend on the employed physical principle. Generally, passive methods are capable of surface defects detection only, while active techniques usually increase the maximum observable

thickness as the energy grows.

Following are briefly presented ([16, 21]) some of the most common NDIs applied nowadays:

1. Optical methods
2. Liquid penetrant
3. Magnetic-particles
4. Radiography
5. Ultrasound
6. Thermography

It should be pointed out that the ability of a test to detect any imperfection is usually strongly related to the experience of the operator who performs the inspection. The know-how is an essential variable to be aware of, and affects both the coupon preparation and analysis as well as data interpretation. Moreover some techniques are more sensitive to a specific type of defect. Thus a unique general testing procedure is not possible, rather different methods are usually complementary.

1.2.1 Optical methods

Optical techniques represent the most intuitive way for crack detection. This kind of inspection is suitable to any kind of material and represents the most cheap and faster surface inspection technique.

Techniques

Optical inspections are capable to find surface defect only, and the minimum detection length varies in the range of 1 - 2 mm for naked eye observation. In addition sensitivity could be increased up to about 0.5 mm if a magnifying lens is used. Other typologies of optical devices (Figure 1.1) are able to increase the sensitivity up to 2.5 μm . These latter generally make use

of optical detectors coupled with a light source, usually combined in an optic fib bundle. The profile projector, for instance, is usually used for observation of inner state blades of turbines.



Figure 1.1: Optical technique. The employment of auxiliary devices could dramatically increase the sensitivity and spot accessibility of the test [10].

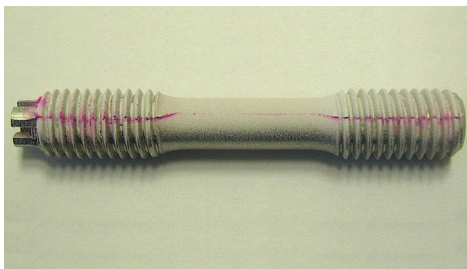
Other systems are also applied, using laser or holographic scans to detect variation of surface in infra-red or white light reflection. Unfortunately, the latter one is not really applicable to composite materials, since an high reflection coefficient is advisable.

Overview

- This method is very cheap.
- It could be applied to any material.
- It is able to detect surface flaws only.
- The size of detectable defects depends on the auxiliary devices employed.
- The result is usually quite subjective and depends on the operator.

1.2.2 Liquid penetrant

Detection of surface defects, especially cracks and leaks, can employ liquid penetrant. The limitation to non-porous material only is a consequence of the particular fluids employed, capable to penetrate inside the surface discontinuities by capillarity (so that would be absorbed by porous material). This method is widely applied since the interpretation of the results is quite objective and clear also for non-experienced operators (Figure 1.2). On the other hand liquid penetrant requires an high level of surface cleaning both before and after the test is performed. It also requires for the component to be disassembled from the structure.



(a) *Red dye penetrant.*



(b) *Fluorescent dye penetrant.*

Figure 1.2: Red and fluorescent dye comparison. It is easy to notice the crack only if the surface is properly cleaned [4, 6].

Techniques

The testing procedure (Figure 1.3) starts with part disassembling. Surface cleaning usually requires solvent and water to wash away any impurity, in particular oil and greases. The following application of dye penetrant is performed by brushing, dipping or spraying and takes several minutes to be absorbed. The excess liquid should be then washed out to avoid background coloration to mask the test outcome. Finally the developer - usually as dry powder - is applied, which recalls the dye penetrant to form a visible indication, the *bleed-out*. The inspection could be done by observation of the component under white or UV light, depending on the type of liquid

used. In general red dye is used to test large parts with rough surface, while fluorescent dye is applied to small and smooth surface components. The defect, if present, is clearly visible as a spot marks.

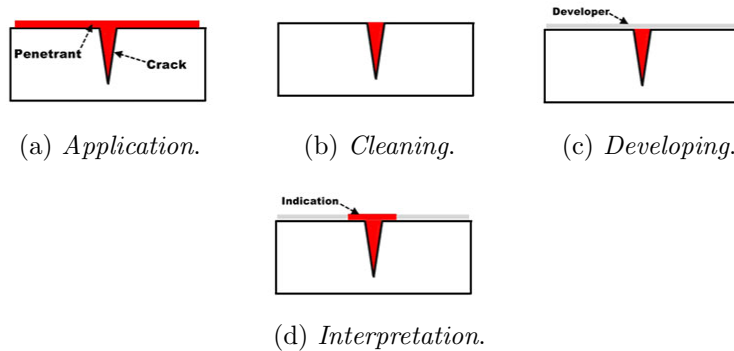


Figure 1.3: Liquid penetrant technique procedure [23].

An important step to be done before part reassembling, is to clean again the component to avoid that residual of dye or developer damages the material.

Overview

- This method is cheap and easily manageable.
- It could be applied to a large variety of non-porous materials.
- It is able to detect surface flaws only.
- The size of detectable defects is dependent on the dye used. Smaller imperfections do not let liquid to penetrate, while larger ones are accessible to water which wash out the liquid.
- The result is quite objective, thus easy to interpret. This implies a low level experienced operators. Otherwise the ability of the operator to a good clean of the surface should be considered.
- Post-testing cleaning is required.

1.2.3 Magnetic-particles

This technique is able to detect surface or sub-surface defects by means of a magnetic powder used as a detector. Since magnetization of the component is required, this method is restricted to ferromagnetic materials only.

Techniques

The magnetic field induction is performed either by magnets - permanent or electro-magnets - or by current. This latter technique may employ continuous or alternated current. The main difference is that DC shows a deeper penetration for the test due to a deeper magnetic field penetration. AC let the magnetic particles be aligned easier, but has a lower penetration. A good compromise is provided by pulsing current (called Half Wave DC) which is capable to join the positive aspects of both methods.

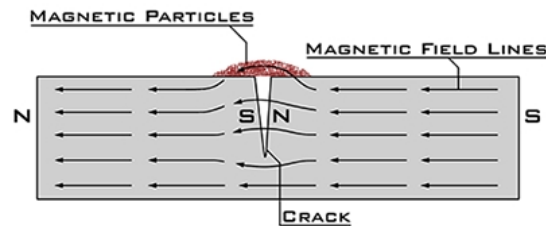


Figure 1.4: Magnetic-particle powder is used as revealing to detect the changing and deflection of the magnetic field lines [27].

Once the part has been magnetized, flaws are detectable since flux leakage due to discontinuities recalls the magnetic particles applied on the surface (Figure 1.4). Thus, the results are quite clear (Figure 1.5). However it should be considered that the effects of deviation of magnetic field lines are felt only for defects not deeper than 2-3 mm. The orientation of defects is important as well, but different layouts can be detected by changing the magnetization orientation. Longitudinal or circular magnetization has to be selected by operator depending on the expected flaw angular orientation (for angles up to 45 degree with respect to surface longitudinal magnetization is used). The

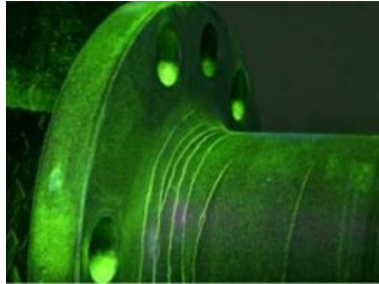


Figure 1.5: Magnetic-particle test is clearly indicating the presence of multiple cracks in this pipe junction [2].

final step required is the de-magnetization of the part, performed either by heating material up to Curie temperature or by hysteresis cycle reduction.

Overview

- This method is cheap and easily manageable.
- It is limited to metallic materials.
- It is able to detect surface or sub-surface cracks not deeper than 2-3 mm.
- The orientation of the flaws with respect to the surface requires different magnetization (longitudinal or circular).
- The result is quite objective and easy to understand. Low level experienced operators could be employed.
- De-magnetization of the part should be performed after testing.

1.2.4 Eddy current

The phenomenon of electromagnetic induction in a conductive material could be exploited to detect and characterize surface and sub-surface (10-15 mm) flaws. This method is applicable to carbon-fiber composites but not to glass-fiber or aramidic ones. Moreover it does not shows particular issues in testing painted parts.

Techniques

First of all an oscillating magnetic field is generated. The frequency is the same as the current running in the coil used to generate it. As the coil approaches to a conductive material, a current - opposite to the external one - is produced inside the material (thus called *eddy current*). Any defect inside the specimen will cause a variation of the electrical conductivity and magnetic permeability thus a modification of eddy current path (Figure 1.6). The detection is performed looking for changes in phase and amplitude with respect to a template, provided by an healthy coupon.

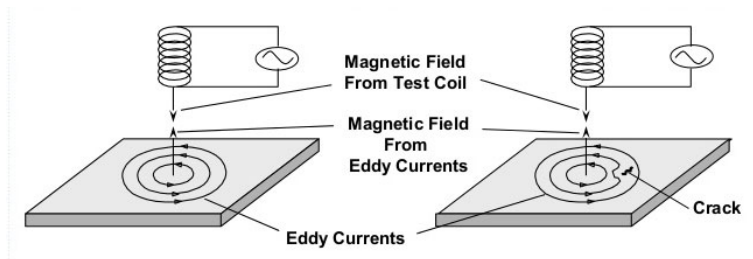


Figure 1.6: Eddy current physical principle. In case of defect eddy current field lines are deviated: [11].

Overview

- This method is cheap and easily manageable.
- It is restricted to conductive materials. Some kind of composites, such as carbon-fiber, could be tested.
- It is able to detect surface or sub-surface cracks up to 15 mm depth.
- Inspection results can be not reliable in complex-shaped specimen, due to alternative paths for magnetic field. The operator experience is fundamental to decide which parts could be tested, which not.
- Rapid and automatable.

As already said, EC is an electrical-based method, thus applicable to conductive materials only. Furthermore eddy current tends to find alternative paths to run, thus introduces issues when observing a complex shaped coupon. An experienced operator is required in this case. Finally, the eddy currents is a quite slow inspection method.

1.2.5 Radiography

Radiography provide one of the most penetrating and advanced NDIs. It is able to detect a defect in many materials at any depth, thus is label as a volumetric technique. This method employs γ or X rays from an atomic source.

Techniques

The basic method for radiography consists in a radiographic film placed behind the coupon which is impressed by the Electromagnetic (EM) beam. The radiation is attenuated with an exponential law, and eventually hits and turns black the film (negative printing), as function of the received radiation. If a defect is present, or there is a variation of the density, the rays will be absorbed more, thus the area will be darker (Figure 1.7). This also introduces a limitation of this method regarding the maximum thickness, but also some complex shapes, of the object to test.

An alternative technique, called radioscopy, is provided by substituting the film with a detector to provide the information on a monitor as a positive printing. This method differs from radiography because is generated by continuous integration of the received data and is not instantaneous.

Both methods provide a 2D image of the part. To locate the defect along the azimuth axis, two different non aligned acquisition of the flaw should be taken. A further development of these methods is the computed tomography, which performs a set of scans from different position in order to provide a

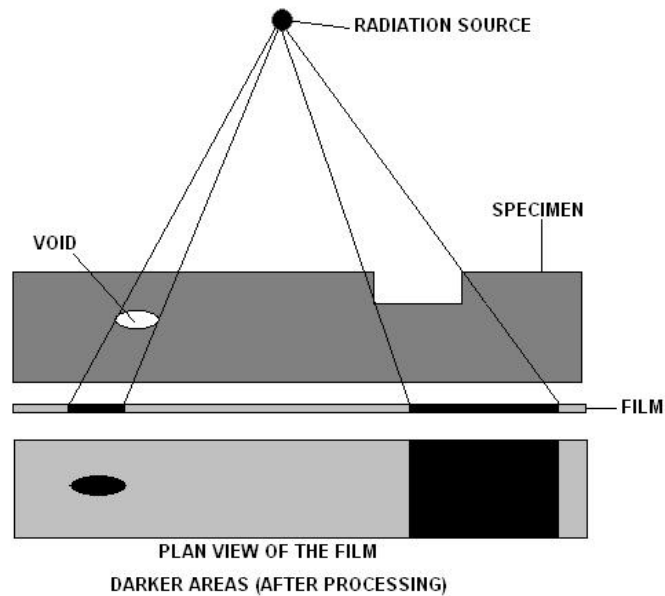


Figure 1.7: Radiography principle [26].

3D reconstruction of the defect with high precision, as shown in Figure 1.8¹.

Overview

- This method is quite expensive, in particular for the equipment.
- It is limited to non-opaque materials having non-complex geometry.
- It is able to detect flaws at any depth.
- Some defects (delaminations and planar cracks) are difficult to detect, thus experienced operators are required.
- Scans must be performed in shielded rooms only. Considering the dimension of equipments, this makes the method be difficult to apply out of designated areas (low transportability).
- The personnel should be certified and require lot of training. Experience is essential to understand the results, but also to handle the

¹Courtesy of: sun.ac.za/CTscanner

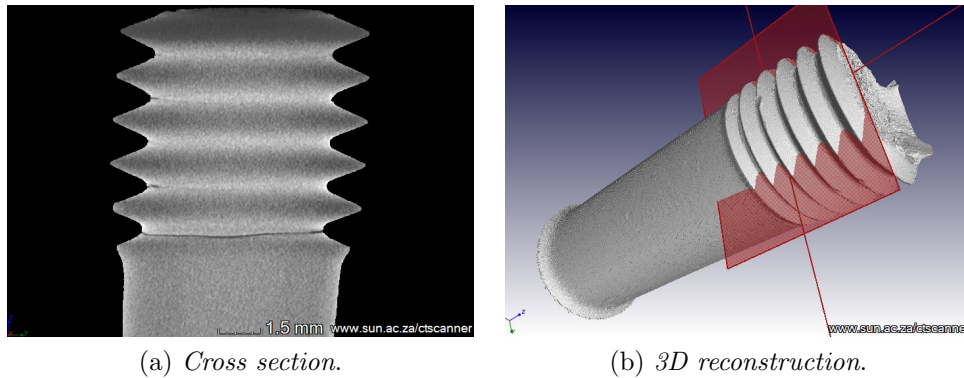


Figure 1.8: Computed Tomography test on a cracked screw.

equipment.

1.2.6 Ultrasound

Ultrasonic testing exploits the sonic wave propagation through the coupon, and the reflection and refraction in correspondence of the possible flaw. It is capable to detect defects inside the coupon no matter how deep are, thus is a volumetric method.

The ability of wave propagation methods to detect flaws depends on wavelengths (thus on frequency) and on size of the discontinuity. As a rule of thumb, a discontinuity is detectable if the size of the flaw is equal or larger than the wavelength. Ultrasonic waves could be longitudinal or transversal and their penetration capability depends on the physical properties of the medium to be analyzed. In particular, the wave should have enough energy to be detected by the receiver transducer, after the attenuation related to the acoustic impedance of the material. Moreover, a part of energy is reflected whenever the wave passes from a medium to another, based on the acoustic impedance ratio of the two materials.

Techniques

The technique employs a simple device with two probes - *emitter* and *receiver* - connected to a generator and an oscilloscope. The waveform is generated at frequencies larger than 1 MHz (typically between 1 and 10 MHz, but occasionally up to 200 MHz) and transmitted by the *emitter*. The wave passes through the coupon and the return is captured by the second probe, the *receiver*. Different probes could be used, depending on the technique applied, among plane, angled, double or immersion one. In fact the discontinuities inside the material could be detected either by getting the defect echo (echo technique) or by getting the attenuated wave which has passed through the whole material (transparency technique). Echo method consists in sending a pulse and measuring its backscatter. The echoes are two in case of healthy coupon, the *start* and *end* echoes. A third peak appears in case of flaw, due to a part of energy being reflected by the discontinuity front, where the variation of the elastic characteristic of the two material - specimen and air - is appreciable (figure 1.9). The depth of flaw can be computed starting from flytime. In a different way, transparency method consists in placing

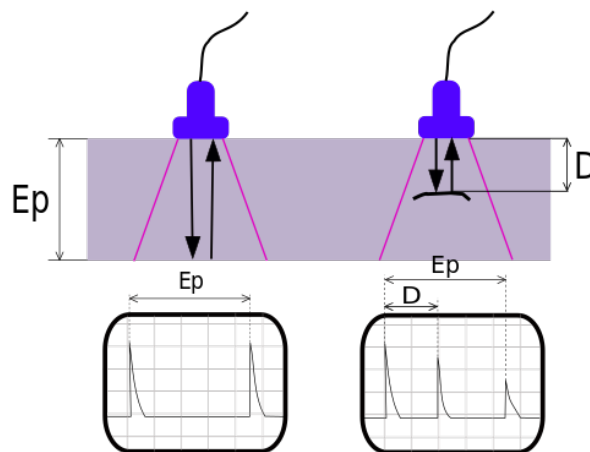


Figure 1.9: Echo technique. On LHS the transducer detects two peaks only, corresponding to the front and rear edges of the specimen. On RHS a third peak appears which represents the echo of the flaw [1].

emitter and receivers on two opposite sides of the specimen. The technique relies on the diffraction of the wave in correspondence of the defects which imply a lower received energy. This method requires a lower execution time due to lower flytime (one-way propagation only). Unfortunately, it is not capable to compute flaw position.

In any cases the received signal is processed considering the waveform amplitude and phase. Flytime could be used to locate the exact position of the flaw, while combining all the parameters to compute received and input wave correlation let the computation of material characteristics and specimen thickness. Three methods could be applied to represent the results:

A-scan provides a representation in the time domain of the received waveform obtained by echo method. It provides information about coupon thickness in addition to flaw depth.

B-scan is a representation of data collected by echo technique on a scan line, which let to show a component cross-section with the possible defects.

C-scan represent an internal 2D view of the part.

In order to have a good scan of the coupon, the layer between probe and specimen should be filled a couplant - usually gel or oil - such to eliminate any trace of air and let the wave propagate in a ultrasonic-semitransparent medium.

Overview

- This method is cheap, in fact is the most-commonly used.
- It is applicable to any material with few limitations regarding low acoustic attenuation and smooth surfaces. Because of that is applicable only to end-of-line testing, but not to raw or semi-finished parts.
- It is able to detect flaws at any depth.
- It is particular effective to detect delaminations and disbonding.

- The method is easily automatable but a proper trained operator is essential for results interpretation.

1.2.7 Thermography

The capability to detect Infrared (IR) radiation intensity is used to depict thermal map of a body. Thermography exploit this principle to detect any local variation of thermophysic properties of a material which could be an indicator of presence of flaws. The application is theoretically possible in any material, but smooth surface requirements restrict the employment only to finished components.

Both active and passive techniques are used. Energy could be provided to the specimen by means of thermal energy, lights or mechanic waves. In the same way the detectors could exploit all this principles. Either *piroelectric* or *photon* detectors are able to generate electronic signals respectively by temperature changes or photons impact. Other systems as *fonodetectors* or *focal plane arrays* perform a surface scan (mechanically or electrically) to map the coupon surface.

Techniques

The application of thermo-cameras allows to detect the object radiation intensity. The measure of the radiation leads to the evaluation of local temperature which is the response of the local material characteristics to any external energy sources. Different methods are used, some active, which introduces specific thermal or mechanic energy sources, others passive which simply record the response to background environment. In case of active methods, monostatic or bistatic test can be distinguished whether the thermal source is on the same side or on opposite with respect to the detector.

The measured variables depends on the type of test performed. Static tests compute thermal resistance, being the thermal flux constant in time. Dynamic ones, have a time-dependent thermal flux, thus the thermal inertia is evaluated. An important type of analysis is the thermoelastic one, which

is the unique method capable to detect humidity inside the materials and it is applicable to any kind of composite.

Following, the major thermography techniques are briefly described.

Thermal Imaging Technique (TIT) is the passive observation of IR radiation of a component (example in Figure 1.10).

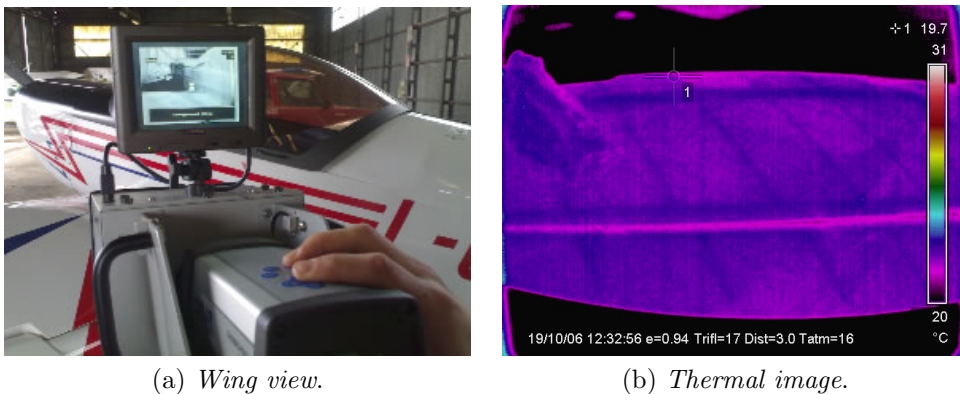


Figure 1.10: Thermal Imaging of a wing. The technique is capable of seeing the internal structure, as spar and ribs in RHS picture [25].

Transient Thermography (TT) performs data acquisition during the cooling transient after the temperature has been increased artificially. Defects are visible as spots in the image, and their depth is computed by the time they first appears on the image.

Photo-thermal Technique (PT) is based on the cyclic thermal stress, induced by flash lamps or ultrasound. After a transient the received thermal signal is compared to emitting source. From response amplitude and phase shift is possible to detect any discontinuity of the material.

Pulse Phase Thermography (PPT) is the observation of the component stimulated by a sinusoidal components flash lights. The response is the same that we would obtain repeating infinite test at different frequencies, as the overall return is the superposition of singular components

response. PPT is much faster than PT since the measurements are performed during the transient.

Microwave Techniques (MT) exploit EM waves emission to heat the coupon. This let internal heating possible and it is particularly effective on polar molecules such as water. Because of that MT is often used to detect traces of humidity inside materials, especially in honeycomb composites.

Overview

- This method is economic, accurate and results are easily repeatable.
- It is applicable to any material with smooth surfaces, it is not suitable to semi-finished components.
- It is able to detect any flaw at any depth.
- Thermoelastic testing can detect the presence of humidity.
- Thermal camera works only in two spectral range 3-5.6 and 8-12 μm , out of the radiation bands absorbed by the atmosphere.
- Operator experience is really important to have an accurate response from data.
- Equipment calibration is frequently required to obtain accurate results.

1.3 Summary

Now that many testing methods have been accessed, it is clear that no such as unique testing method could be used as universal technique. The choice of the method is usually not unique and is left to experienced personnel judgment. Some guidelines can be extrapolated considering the specimen material, expected defect, coupon geometry, desired accuracy and particular requirements (e.g. find the flaw location in the thickness) and of course the pricing of any technique.

The following table is a summary of the most common NDI methods.

Table 1.1: NonDestructive Inspections summary

	Suitable materials	Detectable defects	Advantages	Disadvantages	Penetrating element	Revelator element	Pricing
Optical	Any.	Visible surface damages (scratches, cracks, corrosion, decolorization)	Cheap, if support devices are used damaged area accessibility is easier.	Defect area accessibility.	Sight.	Eye, auxiliary devices (lens, etc).	Very low
Liquid penetrant	Non-porous only.	Surface cracks	Easy, objective results, portable.	Requires high cleaning levels (pre and post)	Fluorescent or visible liquid.	White light or Wood lamp.	Low
Magnetic particle	Metallic.	Surface or sub-surface defect	Applicable on coating.	De-magnetization after testing.	Magnetic field.	Magnetic particles.	Medium - Low
Eddy Current	Conductive (also carbon-fibre).	Surface and sub-surface (up to 15 mm deep).	Rapid, automatable.	Not applicable on complex shape, difficult results interpretation	Electric current.	Oscilloscope	Medium

Table 1.2: NonDestructive Inspections summary (cont.)

	Suitable materials	Detectable defects	Advantages	Disadvantages	Penetrating element	Revelator element	Pricing
Radiography	Any.	Any depth flaws (volumetric test).	Detects flaws at any depth.	Low portability, radioactive danger, not applicable to complex geometries.	X or γ rays.	Film.	Very high
Ultrasound	Any ^a .	Sub-surface or internal (cracks, inclusions)	Automatable, good penetration, good resolution.	Couplant required between probe and surface.	Ultrasonic waves.	Oscilloscope	Low
Thermography	Any ^b .	Any discontinuity in material properties (defects, inclusions, cracks).	Rapid, detect honeycomb in honeycomb.	Very small cracks not visible, requires frequent equipment calibration.	Heat dissipation	Thermo camera	Medium

^aLow attenuation and smooth surfaces are required.

^bSmooth surface is required.

Chapter 2

Radar technology

2.1 Introduction

A Radio Detection and Ranging (RADAR) is a device which radiates some EM power at Radio Frequency (RF) to *illuminate* the surrounding environment and gathers the backscattered power to detect the possible presence of objects (called *targets*) and their distances from the radiating source [20]. Different kinds of radar have been developed since the 1940s when this device was first employed to detect the presence of aircrafts in a observed space. Although surveillance is still the most known application, radars are also employed for weather data monitoring, radio-science data gathering, target detection and imaging.

2.2 Narrow-band radar

A radar is build up in two parts: a transmitting (Tx) and a receiving (Rx) line. Commonly, a single antenna is used both to radiate and receive thus a *duplexer* is used to decouple the two signals.

The transmitting branch processes the signal coming from a *bitsource* and associate a waveform to each bits sequence. Since no information has to be carried all the emitted bits will all be equal. Baseband signal coming from

Pulse Amplitude Modulator (PAM) is combined with the carrier to obtain a RF signal, whose power content is increased using a *power amplifier* and the signal is eventually transmitted by the antenna.

The receiver is slightly more complex. After being received from the antenna, the noise power content is reduced thanks to a *bandpass filter* which clean the signal for the spectral components out of the used bandwidth¹ (W). Downconversion let the frequency pass from RF to baseband by multiplying the signal with a local replica of the carrier provided by the *oscillator*. The processing continues with a *matched filter* tuned to a delayed version ($\tau = t_0$) of the pulse used. The so obtained cross-correlation is then sampled at discrete time and fed to the *detector* which provides the response according on the chosen metrics.

A typical example of a radar block diagram is depicted in Figure 2.1.

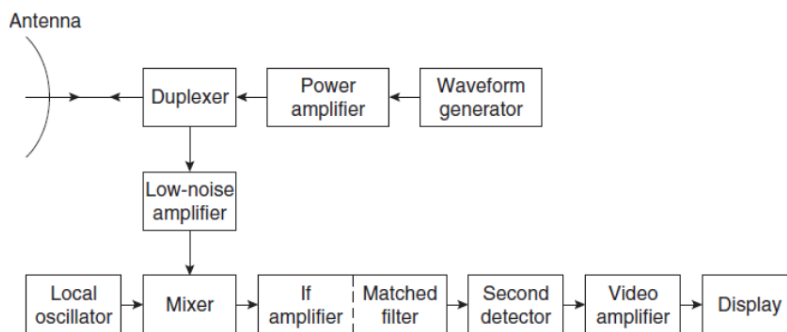


Figure 2.1: A typical representation of a radar block diagram [12].

The performance of a radar system is strongly related to the environmental and background conditions. In fact, apart from the environment noise which requires a low noise amplifier to let the signal be clearly visible in a noisy channel, *clutter* is present too. With this term we denote any undesired echo coming from external sources of the background. These can be atmospheric (fog, rain, ocean, etc...) or due to ground irregularities when

¹If Doppler shift is expected, the band of bandpass filter has to be wider to include all the spectral components of the signal which have changed.

the beam is almost parallel to it.

The study of a radar system involves a large set of system parameters and problem variables. Two parameters are particularly important to evaluate the radar performance:

- Radar Cross Section;
- Radar range.

Radar Cross Section (RCS) is defined as the section of an equivalent sphere which causes the same backscattered power of the investigated object.

$$\sigma = \frac{P_s}{p_i} \quad (2.1)$$

where P_s is the power scattered back from the target (measured in W) and p_i is the incident power density (measured in $\frac{W}{m^2}$). In general, RCS depends on the carrier frequency of the emitted signal (f_0) as well as on material and geometry properties of the target, in fact

$$\sigma = F(f_0, \theta_i, \phi_i, \theta_s, \phi_s)$$

where (θ_i, ϕ_i) is the incident direction and (θ_s, ϕ_s) the scattering one.

Some materials are capable to reflect power better than others, moreover some particular geometries, such as multifaceted body, could reflect power in many different directions reducing the backscatter power directed to the source².

To compute the *radar range*, let us introduce the radar equation:

$$P_r = A \frac{P_t G^2}{(4\pi)^3 r^4} \left(\frac{c}{f_0} \right)^2 \quad (2.2)$$

where:

A is the attenuation factor, accounting for polarization, power adaptation and supplementary losses (always < 1);

²Low reflection materials and sharp geometries are typically used in *stealth aircraft*.

P_r is the received power [W];

P_t is the peak transmitted power [W];

G is the antenna gain³ [dBi];

r is the target distance [km];

f_0 is the carrier frequency [GHz].

From (2.2) is clear that received power decays with the fourth power of the distance and the square of the emitted power, thus very high power (in the order of MW) should be used. On the other hand it may seem that the received power decreases with the square of the carrier frequency, but considering the implicit relation $G \propto f_0^2$, it turns out that also $P_r \propto f_0^2$. High carrier frequencies are thus employed, usually in the order of a few GHz.

Starting from radar equation one may compute the maximum range a target can be detected. Assuming that a minimum received power exists to allow target detection, such that the Signal to Noise Ratio (SNR)⁴ is still lower than some threshold, thus the maximum range for detection is expressed by the radar range (2.3).

$$r \leq \sqrt[4]{\frac{P_t G^2 \sigma}{KT_{syst} W (4\pi SNR_{min})^3} \left(\frac{c}{f_0}\right)^2} \quad (2.3)$$

where $KT_{syst}W$ is the noise power, being:

K the Boltzmann constant;

T_{syst} the equivalent noise temperature [K];

W the signal band [Hz].

The signal emitted by a narrowband radar is typically a short time duration pulse with very low duty cycle (usually a sine lobe). This let the system have

³In case of monostatic configuration. If the radar is a bistatic one, thus we have two separated antennas with different gains, G^2 should be substituted by $G_{TX}G_{RX}$

⁴SNR is the ratio between the useful power and the noise one, i.e., $SNR = \frac{P_{signal}}{P_{noise}}$

a good resolution. If bandwidth constraints are imposed, the duration of the pulse may be changed to accomplish the requirements.

2.3 UWB radars

The information content of a narrowband signal is very limited, since the amount of data transmitted per unit of time is proportional to the signal band. As a consequence, increasing the band implies increasing the information content of the signal. Ultra-Wideband data rate is much higher than traditional narrowband communication system due to the very large band employed. On the other hand, coexistence with other communication system operating in the same band is possible, since UWB has restriction on transmitted power (see Section 2.3.1).

Some differences with respect to a conventional radar are following listed:

- Improved target ranging;
- Possibility to perform target identification, thanks to different components visibility provided by the higher information capability;
- Reduced clutter and interference from atmospheric phenomena and electromagnetic sources;
- Increase probability of target detection, in particular for low elevation angles (ground clutter can be isolated);
- High capability of material penetration, thanks to the large range of employed frequencies;
- Possible employment for human health monitoring (heartbeat, breath, presence detector, *etc.*...) thanks to low power emitted and high resolution.

An important difference with respect to classic narrow-band radar is represented by signal processing. Although in narrowband radar target reflection is able to modulate any signal parameter, in UWB radar also the signal

shape will change. Since no *a priori* signal waveform information is known, UWB signal conventional processing methods, such as match filtering and signal correlation, become challenging to implement. Since the signal shape could change, the received waveform processing is usually performed in the time domain for any UWB device, despite it is conventionally done in the frequency domain for classic radars.

A great difference between UWB and conventional radars is the concept of RCS introduced in (2.1). Since UWB RCS is time-dependent, the concept of instantaneous RCS is provided.

$$\sigma_{UWB} = \sigma(t)$$

It is clear that the definition of radar range also becomes a function of time, and may be written as follows:

$$r_{UWB}(s, t) \leq \sqrt[4]{\frac{EG(\theta, \phi, S, t)\sigma_{UWB}(t)A(\theta, \phi, S, t)}{(4\pi)^2\rho q N_0}}$$

where E is the energy radiated signal, ρ the system losses, q the threshold SNR and N_0 the noise power spectral density.

2.3.1 UWB regulation

Several formal definitions for UWB devices actually exist. On both sides, US and EU rules have been developed to restrict the unlicensed employment of UWB radar devices. Actually, three different regulations define a UWB device and its employment.

- IEEE STD 1672 *Ultrawideband Radar Definitions*;
- US Federal Communications Commission (FCC) *Title 47 part 15* [24]⁵;
- EU Commission Decisions⁶ of *21 April 2009* [7] and *7 October 2014* [9]

⁵www.law.cornell.edu/cfr/text/47/part-15

⁶eur-lex.europa.eu

(amending *Decision 2007/131/EC* [8]).

Definitions

The EU regulation defines an UWB device as follows:

equipment using ultra-wideband technology means equipment incorporating [...] technology for short-range radio communication, involving the intentional generation and transmission of radio-frequency energy that spreads over a frequency range wider than 50 MHz [...]

Whilst FCC provides the following definition of UWB transmitter:

An intentional radiator that, at any point in time, has a fractional bandwidth equal to or greater than 0.20 or has a UWB bandwidth equal to or greater than 500 MHz, regardless of the fractional bandwidth.

For sake of clearance, UWB parameters are herein reported, as defined in European regulation 2007/131/EC and following amendments.

With **UWB bandwidth** is denoted the *frequency band bounded by the points that are 10 dB below the highest radiated emission, as based on the complete transmission system including the antenna. The upper boundary is designated f_H and the lower boundary is designated f_L . The frequency at which the highest radiated emission occurs is designated f_M .*

Thus

$$W_{UWB} = (f_H - f_L)$$

On the other hand, the **fractional bandwidth** is defined as the ratio between the bandwidth and the central frequency $f_C = (f_H + f_L)/2$ (not necessary equal to the peak frequency f_M):

$$W_f = \frac{W_{UWB}}{f_C} = \frac{2 \cdot (f_H - f_L)}{f_H + f_L}$$

The regulation also defines several power parameters, which are eventually used to introduce limitations on devices.

The **EIRP** is defined as *Equivalent Isotropically Radiated Power, i.e., the product of the power supplied to the antenna and the antenna gain in a given direction relative to an isotropic antenna.*

Maximum mean power spectral density *specified as EIRP of the radio device under test at a particular frequency, is the average power per unit bandwidth (centred on that frequency) radiated in the direction of the maximum level under the specified conditions of measurement.*

Peak power, *specified as EIRP, contained within a 50 MHz bandwidth at the frequency at which the highest mean radiated power occurs, radiated in the direction of the maximum level under the specified conditions of measurement.*

Application fields

The regulation provides a set of typical and allowed application fields as well.

Surveillance for short-range application;

Wall and through-wall based on the high information content and on deep penetration, UWB is capable to map surfaces and materials inner layer (used for material building application);

Imaging in particular for medical employment, thanks to high resolution and low radiations level.

In this latter category we found SAR devices, which are the topic of this work. A technical description of these devices is provided in Section 2.5.

Restrictions

The restrictions on the employment of UWB radar are mainly related to transmitted or peak power in order to avoid this UWB devices to jam other narrow band devices frequencies. EU Commission Decision 2007/131/EC yet

established some EIRP limits, depending on the central frequency used, for those devices without any mitigation technique applied. On the other hand amendment 2009/343/EC further introduced different peak and mean EIRP limits based on the UWB devices application fields (Table 2.1). Moreover it introduced two different mitigation techniques, which are Low Duty Cycle (LDC) or Detect and Avoid (DAA).

Table 2.1: Generic UWB usage power restriction (2014/702/EU).

Technical requirements		
Frequency range	Maximum mean power spectral density (e.i.r.p)	Maximum peak power (e.i.r.p) (defined in 50 MHz)
$f \leq 1,6$ GHz	- 90 dBm/MHz	- 50 dBm
$1,6 < f \leq 2,7$ GHz	- 85 dBm/MHz	- 45 dBm
$2,7 < f \leq 3,1$ GHz	- 70 dBm/MHz	- 36 dBm
$3,1 < f \leq 3,4$ GHz	- 70 dBm/MHz or - 41,3 dBm/MHz using LDC or DAA	- 36 dBm or 0 dBm
$3,4 < f \leq 3,8$ GHz	- 80 dBm/MHz or - 41,3 dBm/MHz using LDC or DAA	- 40 dBm or 0 dBm
$3,8 < f \leq 4,8$ GHz	- 70 dBm/MHz or - 41,3 dBm/MHz using LDC or DAA	- 30 dBm or 0 dBm
$4,8 < f \leq 6$ GHz	- 70 dBm/MHz	- 30 dBm
$6 < f \leq 8,5$ GHz	- 41,3 dBm/MHz	0 dBm
$8,5 < f \leq 9$ GHz	- 65 dBm/MHz or - 41,3 dBm/MHz using DAA	- 25 dBm or 0 dBm
$9 < f \leq 10,6$ GHz	- 65 dBm/MHz	- 25 dBm
$f > 10,6$ GHz	- 85 dBm/MHz	- 45 dBm

2.4 Novelda NVA6201 radar overview

The UWB radar employed during this work is the Novelda impulse radar transceiver NVA6201 [18]. The development kit is built up of a radar module, a set of two antennas and an I/O module (Figure 2.2). The interface between the I/O module and the custom software (developed in Matlab) is provided by Novelda RadarLib3 as driver set and a software sublayer. The basic configuration for the radar is a bistatic, where the transmitter and receiver antennas are 150 mm far from each other⁷.



Figure 2.2: The Novelda radar NVA6201 with antenna lens [18].

The impulse generated by the chipset is a high order Gaussian pulse (derivative of the Gaussian pulse, see Figure 2.3). Thus, a RF signal is generated without using any sinusoidal carrier thanks to high frequency obtained by the oscillation of the pulse itself. The frequency of the pulse is programmatically set through the value *PGSelect*. As a consequence of the generation principle, selecting higher central frequency will provide a shorter time-domain signal, but the bandwidth will also be lower. During the test campaign, it was set *PGSelect=5* to have a central frequency of 6.8 GHz with a bandwidth of 2.3 GHz. Using this parameter, the duration of the pulse was about 1.3 ns.

Other values set during the test campaign are resumed in Table 2.2. These settings have been chosen based on the description provided by RadarLib

⁷Actually this configuration has been modified to enhance the system, see Section 3.2.

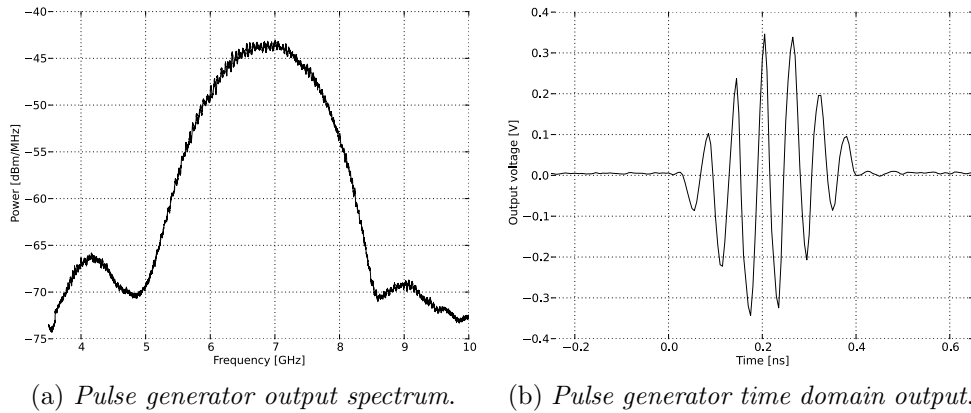


Figure 2.3: Novelda NVA6201 generated radar pulse. The high frequency is generated through an oscillating waveform represented by higher order derivative of Gaussian pulse, rather than using a carrier [19].

datasheet [19] according to the requirements of range visibility.

Table 2.2: Novelda radar settings.

Parameter	Value	Notes
PGSelect	5	$f_0 = 6.8$ GHz, $W = 2.3$ GHz.
SamplersPerFrame	256	
FrameSize	$7.11 \cdot 10^{-9}$	[s]
SamplersPerSecond	36	$f_s = \frac{256}{7.11 \cdot 10^{-9}} = 36$ GHz.
PulsesPerStep	100	
FrameStitch	1	
OffsetDistanceFromReference	0	[m]
SampleDelayFromReference	$2.67 \cdot 10^{-9}$	[s] (=0.800 m cable delays).

The specifications for the set values are herein briefly described.

PGSelect sets pulse frequency f_0 , and as consequence the bandwidth W .

SamplersPerFrame is the number of samples in one frame.

FrameSize sets the length of observation window, in seconds.

SamplersPerSecond is the sampling frequency, constrained by the values of samples in one frame and frame duration $f_s = \frac{\text{SamplersPerFrame}}{\text{FrameSize}}$.

PulsesPerStep is the value of transmitted pulse.

FrameStitch sets the number of frames to be stitched together.

OffsetDistanceFromReference defines the distance of reference point, starting from the radar.

SampleDelay is the sum of `SampleDelayFromReference` and `SampleDelayToReference` and express the delay from the begin of acquisition and sampling.

2.4.1 Antennas

Novelda starter kit is equipped with a set of Sinuous antennas. The highly directionality of these antennas provides quite a narrow beam. The application of dielectric lens further increases the gain to 6.7 dBi and lowers the opening angle to 40 deg (vertical) \times 35 deg (horizontal), almost half of the original one. This opening angle is computed from the antenna radiation pattern provided in Figure 2.4 at -3dB which provides a loss in power equal to half of the peak one. The advantages of having a narrower beam will be clear in Section 3.1.

2.5 Synthetic Aperture Radar

Synthetic Aperture Radar (SAR) is a radar-based method which exploits the scene scanning by continuously moving the antenna beam. The observation of targets from different position is then used to reconstruct a 2D map of the scene reflectivity [3]. SAR imaging represents an *active* technique, widely employed in satellites or aircraft devices to map some ground areas.

2.5.1 Scanning process

Conventional strip-mode SAR imaging employs an antenna moving along a straight path, collecting waveforms at different time. The signals reflected

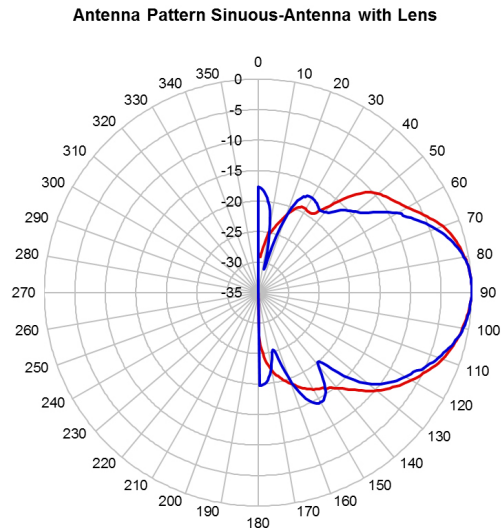


Figure 2.4: Antenna radiation pattern (with lens) obtained in anechoic chamber at $f_0 = 7.25\text{GHz}$. Both vertical (blue curve) and horizontal (red curve) pattern are shown between 0° and 180° [17].

by any of the radar scatter sources (called *scatterers*) is an attenuated replica of the signal, delayed by the roundtrip travel time. The delay is detected both in the position of the received pulse and phase of the signal carrier.

The scatterers providing their contribution to the instantaneous acquired signal are those which are located, time by time, in the footprint of the radar (Figure 2.5). Several scatterers could be present in a given area, thus the overall signature will be provided by the coherent superposition of their echoes. In fact, the backscatter coefficient σ^0 could be expressed as the sum of the RCSs of all the objects present normalized by the observed area (A), such to express the mean power reflected per unit area.

$$\sigma^0 = \frac{\sum_n \sigma_n}{A}$$

Data depend on two variables, namely time and position along the flypath.

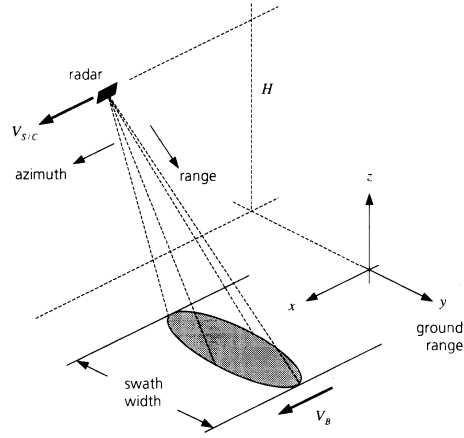


Figure 2.5: Side looking radar imaging geometry. (from [3])

2.5.2 Resolution

In order to distinguish objects radially separated by a distance δ_R , it should be verified that

$$\delta_R \geq \rho_R = \tau_p c / 2$$

where $\tau_p = 1/\Delta f$ is the pulse duration, c is the speed of light and ρ_R is called *range resolution* which define the minimum range separation to detect two different targets. It is now clear that lower duration pulses let us have higher range accuracy.

Furthermore it can be also demonstrated that the *azimuth resolution* is half of the width of the main lobe [5] that is

$$\rho_x = L/2$$

where L is the antenna length. In particular, due to SAR device movement, the effective length of the synthetic array is provided by the distance covered which is equal to the width of the footprint

$$L_{eff} = 2\lambda R_0 / L$$

where R_0 is the range and the value $2\lambda/L$ represents the beamwidth of the antenna.

2.5.3 Processing

The echo signals are stored into a raw data matrix to be eventually processed. The capability to reconstruct a 2D image relies on the *coherent* combination of the waveforms acquired (i.e. detecting amplitude and phase of the echo signal by quadrature demodulation).

Since high bandwidth pulses are usually employed instead short ones, a *range compression* procedure is performed. It consists of signal correlation with a replica of the transmitted waveform so that range resolution becomes $\rho_R = c/(2W)$. Although this is generally performed for a large variety of pulse waveforms, the procedure is different for the most commonly used *chirp* pulse. In the *upchirp* pulse the frequency is linearly increasing with time, thus the wave is divided in several frequency components, which are eventually superimposed in the compression process.

2.5.4 Image properties

The image generated by SAR processing is not a true color image. It does not represent an optic view, but the map of EM reflectivity of the scene. Image matrix pixels are not a non-negative real-valued, instead their value could be negative and even complex-valued. This depends on the computational approach used to associate the value to any pixel.

Assume the image matrix $I(j, k)$ possibly complex-valued. Define *amplitude* its modulus $|I(j, k)|$ and *pixel intensity* $i(j, k) = |I(j, k)|^2$. Although the amplitude does not have any straightforward physical meaning, the intensity is related to the backscattered energy.

Unfortunately SAR imaging is highly dependent on sensor position. Bad geometric conditions may lead to distortion of the mapped scene as *foreshortening* occurring in Figure 2.6. The mountains on the RHS appear to be

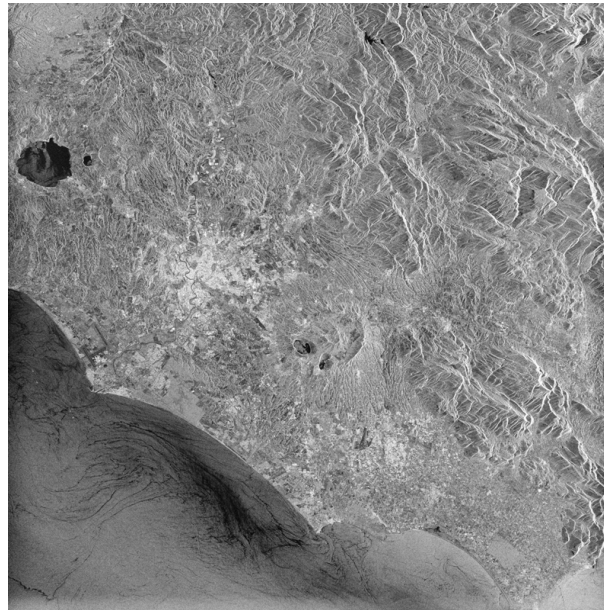


Figure 2.6: ESA ERS-2 image of Rome, Italy (Sept 2011). ©ESA

stretched due to the slopes tilted away from sensor, thus *radar shadow* also occurs in the terrain behind the mountains.

Chapter 3

System development

3.1 SAR application

The purpose of this thesis is to create an autonomous system defect detection and reconnaissance. The system has to provide data acquisition and post-processing analysis up to the decision whether a defect is present, and eventually identify it based on a previously compiled database. A critical step is represented by the computation of the image pixels values, which is based on a literature research of analogous problems faced in other fields. A pronounced similarity with minefield scanning [22] and head stroke detection [14] provides an interesting approach to be developed in Section 3.5.

The design includes a scanning procedure to acquire the raw data matrix containing the waveforms from the radar which will be then pre-processed to obtain a coherent set of waveforms providing a full picture of the scene. The image is then computed based on an appropriate algorithm. Once a suitable database of defects has been compiled, each new acquisition, after processing, is compared to the database to provide information about already known defects.

3.2 Setup

The radar is placed on its own support [12] which is able to move along two axes over an area of about 300×250 mm. The specimen (a plate) is positioned in front of the support.

A monostatic radar configuration is preferable, thus the two antennas have been positioned close to each other by moving the receiving antenna closer to the transmitting one and connecting it with a cable (RG58 coaxial). The cable additional delay compensation is provided by shifting the radar observation window through *SampleDelayFromReference* parameter. The value of delay is computed by solving the equation

$$dt = \frac{L}{c - v_{cable}}$$

where $L = 0.6$ m is the cable length and v_{cable} is the wave velocity inside the cable. This latter is computed as

$$v_{cable} = \frac{c \cdot Z_0}{\log(b/a)}$$

where $Z_0 = 50 \Omega$ is the cable resistance, $a = 0.405$ mm is the outside radius of inner conductor and $b = 2.5$ mm is the inside radius of the outer conductor (Figure 3.1).

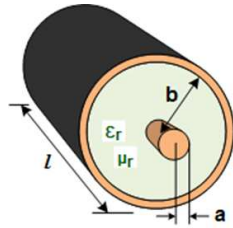


Figure 3.1: Cable dimension scheme.

The new configuration is characterized by a reduced antennas distance. In fact the reciprocal distance was reduced from 15 cm to 4.5 cm (center to center). The distance to the specimen is 0.230 m such that the cross-talk

and the backscattered pulse are not superposed in the return signal.

3.3 Acquisition

The scanning algorithm provides a 2D matrix containing the waveforms corresponding to the observed scenario. The plate is scanned moving the radar device by 1 mm steps in a zig-zag pattern, so that an entire square area of 100 mm length is covered. A detailed view of the path followed, is shown in Figure 3.2a. Thus the gathered data consist of a 2D matrix

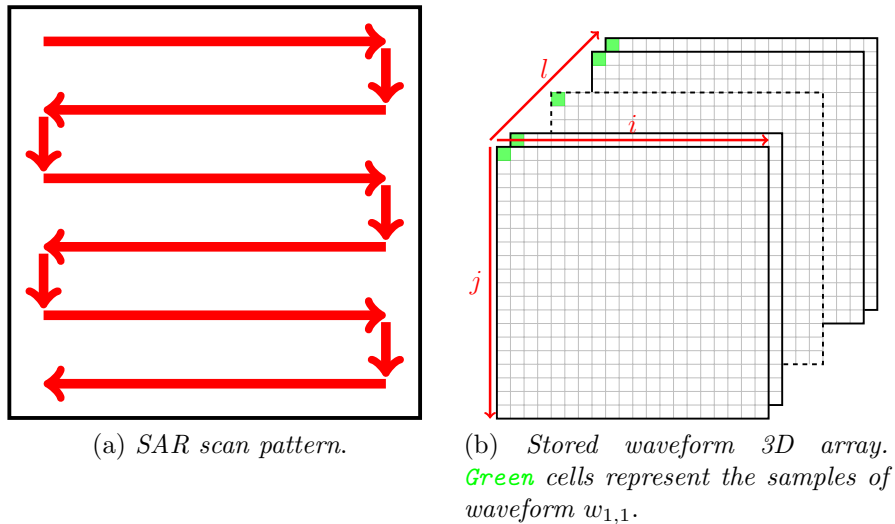


Figure 3.2: SAR scan pattern and waveform storage.

of waveforms, each one identified by a pair of indexes (i, j) where i is the column index and j the row index representing the position at which the waveform has been acquired. In order to store these data a 3D array is used, where the additional index l , completing the set (i, j, l) , represents the sample index, as depicted in Figure 3.2b. Since Novelda radar provides 256 samples (Table 2.2), data are stored in a $100 \times 100 \times 256$ three-dimensional matrix of floating point values in double precision.

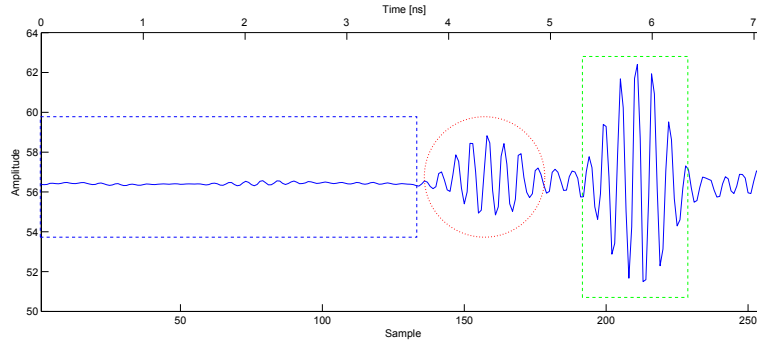


Figure 3.3: Typical acquired waveform. **Blue**: environmental noise; **red**: cross-talk; **green**: backscattered pulse.

Figure 3.3 illustrates an example of acquired waveform. It worth providing the distinction of different regions. Samples of index less than 130 represent the environment noise acquired by the receiving antenna. On the other hand, in correspondence of samples with index between 130 and 170 the so-called *cross-talk* is visible. It represents a part of the pulse radiation which directly travels from transmitting to receiving antenna. It has the same pulse shape whilst the intensity as well as the temporal position depends on the distance between antennas. The cross-talk is usually an undesired effect, but it turns out to be very useful in this application, as explained in the following section. Finally samples whose index range from 180 to 230 represent the backscattered pulse coming from the specimen.

3.4 Preliminary data processing

During the pre-processing waveforms are upsampled, aligned, and prepared to be coherently used in the imaging algorithm. This part of the algorithm is divided into three steps: *resampling*, *pulse correlation* and *signal realignment*.

3.4.1 Resampling

The very first step consists of waveform resampling. This operation is required since the receiver samples the time-continuous received signal. Although the radar sampling frequency is higher than the Nyquist frequency¹, the samples provided by the radar do not necessarily correspond to the original signal peaks, which may jeopardize the realignment operation. The resampling is an operation which allows to obtain an higher number of samples for the original continuous signal, as shown in Figure 3.4. The value of

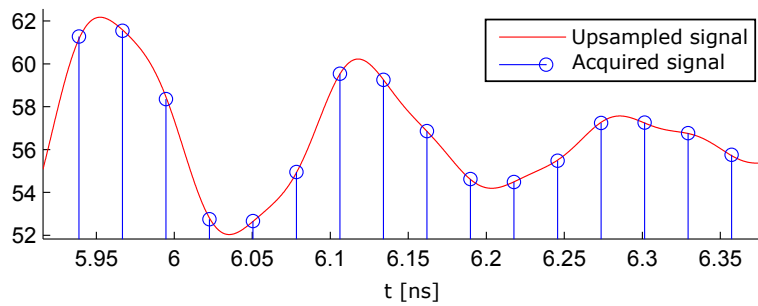


Figure 3.4: Example of FFT resampled signal.

resampling ratio is a tradeoff between a fine temporal accuracy (high values) and resampling computation time (low values) which finally turns the choice to

$$k_{resampling} = 150.$$

Different algorithms may be used, among which we used the Fourier transform resampling because it provides satisfactory results in a restricted time interval and with quite low computational effort.

The Fourier transform method consists of the separation of the Fast Fourier Transform (FFT) of the signal in two parts of equal length ($256/2 = 128$). The two parts of the signal are placed respectively at the beginning

¹Nyquist-Shannon sampling theorem assures that, given an analog signal $s(t)$ whose bandwidth is limited by the upper frequency f_m , the signal may be univocally reconstructed starting from its samples $s(n\Delta T_s)$ if the sampling frequency $f_s = \frac{1}{\Delta T_s}$ is $f_s > 2f_m$.

and at the end of a new array of length equals to the number of desired samples, i.e. $256 \cdot k_{resampling}$, and all the others values are set to 0. Assuming $V = [V_1 \dots V_{256}]$ to be the acquired signal row vector and $V^1 = FFT[V]$, thus

$$V^2 = [V_1^1 \dots V_{128}^1 \underbrace{0 \dots 0}_{256 \cdot 149} V_{129}^1 \dots V_{256}^1]$$

The resampled signal is thus provided by the real part of the inverse Fast Fourier Transform (iFFT) of the waveform V^2 multiplied by $k_{resampling}$, to correct for the amplitude reduction due to the expansion of the row vector. Considering settings provided in Table 2.2, which gives an original samples separation of

$$dt = \frac{7.11 \cdot 10^{-9}}{256} s \approx 27.77 ps$$

the resampled signal samples separation will be 150 times lower, meaning

$$dt = \frac{27.77 \cdot 10^{-12}}{150} s \approx 0.185 ps$$

which corresponds to a spatial separation of 0.055 mm (whilst the original one was 8.325 mm). If two objects are closer than this value, they will probably be identified by the same point on the waveform, thus they will not be distinguished. This will be really important to define the reference for any pixel in Section 3.5.

3.4.2 Pulse convolution (Matched filtering)

After resampling, a substantially larger number of signal samples is available, better identifying the positions of the peaks (since the peaks are not cut-out by the original sampler). As we have discussed in Section 2.3, the UWB pulse shape could change also after signal reflection. Although, we may provide a first signal filtering which gives a measure of the likelihood between the received signal and a time scrolling version of the generated pulse². This

²Generated pulse is assumed to be similar to the backscattered pulse from an healthy plate.

step is similar to cross-correlate the signal and the pulse, but the herein used function, provides the likelihood of the signal with respect to the pulse as it is shifted in time. The operation is obtained using a Linear and Time Invariant (LTI) filter to compute the convolution between the acquired and realigned waveform $w^r(t)$ and the pulse $p(t)$, namely,

$$\begin{aligned} w(t) &= w^r(t) * p(t) \\ &= \int_{-\infty}^{+\infty} w^r(\tau)p(t - \tau)d\tau \end{aligned} \quad (3.1)$$

Filtering is performed in the time domain, and the output signal $y(t)$ has the same number of samples as the sum of samples of the two processed signal minus one to have the signal always overlapped.

The aim of this step is to perform a pulse compression making the received signal more suitable to generate an image. It has been verified that the convolution process slightly compresses the pulse energy even if this is not fully evident from Figure 3.5. In fact, the filtered signal is even more oscillating than the previous one, but the peaks amplitudes are much more clearly separated. Although filtering would result more effective for narrow-band waveforms, its beneficial effects are appreciable also for UWB pulses.

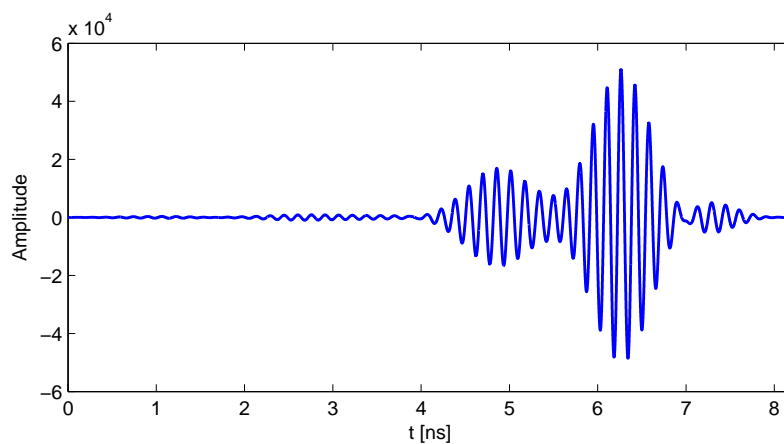


Figure 3.5: Waveform after filtering.

The particular LTI filter used to perform the cross-correlation computation is called Matched Filter (MF). The peculiarity of this operation is that if the filter is matched to the pulse $p(t)$, its response is the convolution with a conjugate time-reversed version of the template. Thus, let the MF transfer function be $H(f) = P^*(f) \cdot e^{-j2\pi t_0}$ for some t_0 . The filter output signal to the input $w^r(t)$ may be expressed as

$$\begin{aligned}
 y(\tau) &= \int_{-\infty}^{\infty} w^r(\xi) \cdot h(\tau - \xi) d\xi \\
 &= \int_{-\infty}^{\infty} w^r(\xi) \cdot p^*(t_0 - (\tau - \xi)) d\xi \\
 &= \int_{-\infty}^{\infty} w^r(\xi) \cdot p^*(\xi - (\tau - t_0)) d\xi \\
 &= \mathcal{C}_{w^r,p}(\tau - t_0).
 \end{aligned} \tag{3.2}$$

Therefore, processing a waveform with a filter matched to the pulse, provide their cross-correlation function, as depicted in Figure 3.6.

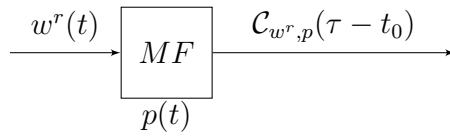


Figure 3.6: Matched filter behavior.

3.4.3 Realignment

So far, the waveforms acquired in each point have been processed separately. From now on, they have to be combined, hence they need to be perfectly aligned in the time domain. The starting point alignment provided by Novelda is dependent on both clock stability and processing delays. Thus a realignment of the acquired waveforms could be necessary. To this aim some absolute time reference is useful. Return pulse is not suitable at all, since it contains scene information and it is dependent on scene set. On the other hand, the cross-talk represents an absolute reference depending on antennas reciprocal position, and does not change during the scanning.

Using the cross-talk cross-correlation of all the waveforms with respect to a reference one, for instance the first acquired one, a delay matrix is computed.

The principle applied to compute the delays matrix values is based on cross-correlation, as it represents a measure of the similarity of two signals. If two similar waveforms are compared (restricted to their cross-talk section) their correlation will have a peak in a position depending on both their shapes. The delay $d_{i,j}$ associated with the resampled waveform $w_{i,j}^r$ can be obtained by taking the difference between the peak of correlation between the waveform and the reference one, and the peak of autocorrelation of the reference waveform, i.e.,

$$d_{i,j} = \arg \max_l \mathcal{C}(w_{i,j}^r|_{\text{crosstalk}}(l), w_{1,1}^r|_{\text{crosstalk}}(l)) - \arg \max_l \mathcal{R}(w_{1,1}^r|_{\text{crosstalk}}(l))$$

where l is the sample index.

Once the delay matrix has been computed, in order to align all waveforms a time shift is performed. Hence the computed time delay is applied to each signal obtained from the convolution as

$$s_{i,j}(t) = w_{i,j}(t - d_{i,j}).$$

3.5 Image formation

In this section the preprocessed waveforms computation procedure is explained in details. However, a short introduction shall be supplied to the reader in order to provide the knowledge about the system theoretical background and to highlight the simplicity of the idea at the basis of this work. Those who are already experienced in SAR image processing could skip Subsection 3.5.1 without hesitations.

3.5.1 Introduction

Although we are dealing with a UWB radar, it is much more convenient to explain the background idea behind the image formation algorithm by means of a very narrow pulse. For sake of clearance, let us assume to have a Dirac discrete delta pulse also known as Kroneker delta pulse defined as

$$\delta_{ij} = \begin{cases} 1, & \text{if } i = j \\ 0, & \text{if } i \neq j \end{cases}$$

which is represented in Figure 3.7.

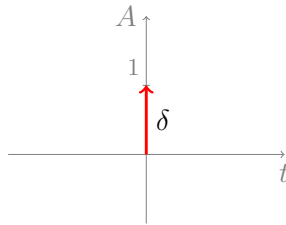


Figure 3.7: Kroneker delta pulse.

If we place a target in front of the radar, the backscattered received signal will be an attenuated version of the transmitted pulse (Figure 3.8b), delayed by a time amount

$$\tau = \frac{2d}{c}$$

being c the speed of light and d the target distance radar-target in Figure 3.8a.

Nevertheless if any flaw is present on the target, such it is not completely flat, this behaves as a scatterer, whose reflection is usually of lower power content with respect to the complete target. This causes some further peaks to appear. In case of a single defect, a single *defect scattering* pulse shape is received, which is temporally separated from the target pulse backscattered by a delay Δt (Figure 3.9b).

In principle the delay Δt between those two peaks could be calculated by

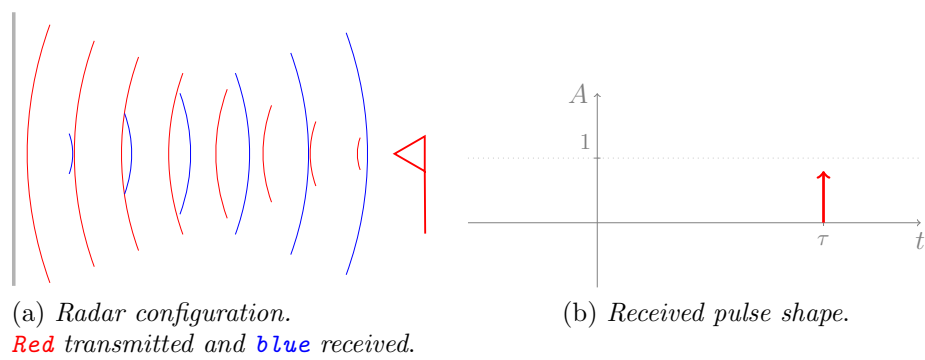


Figure 3.8: Radar - plate configuration.

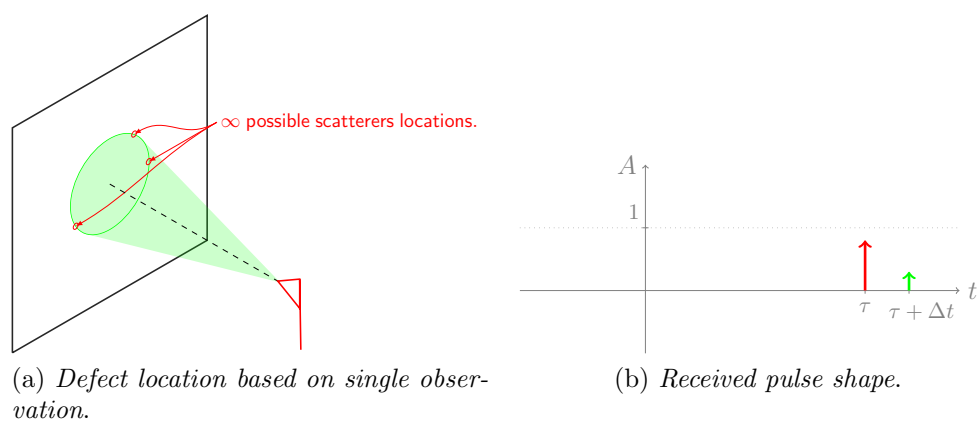


Figure 3.9: Radar generic configuration.

the knowledge of the problem geometry. Despite of that the inverse problem, i.e., the location of the defect on the plate, is not in general solvable exploiting a unique observation. This is due to the fact that the extra fly-time given by Δt let the defect be located on a circumference of centre in the azimuthal projection of the radar on the plate as shown in Figure 3.9a. Not even a second acquisition with the radar in a different position could help solve the uncertainty, but it only restricts the location of the scatterer among the points P_1 and P_2 which are the two intersections between the circumferences $\mathcal{C}_1 \cap \mathcal{C}_2$ (Figure 3.10a) whose centers are in the radar position projections on the plate whilst the radii are functions of Δt_1 and Δt_2 respectively (Figure 3.10b). In order to solve the location of a point, a mini-

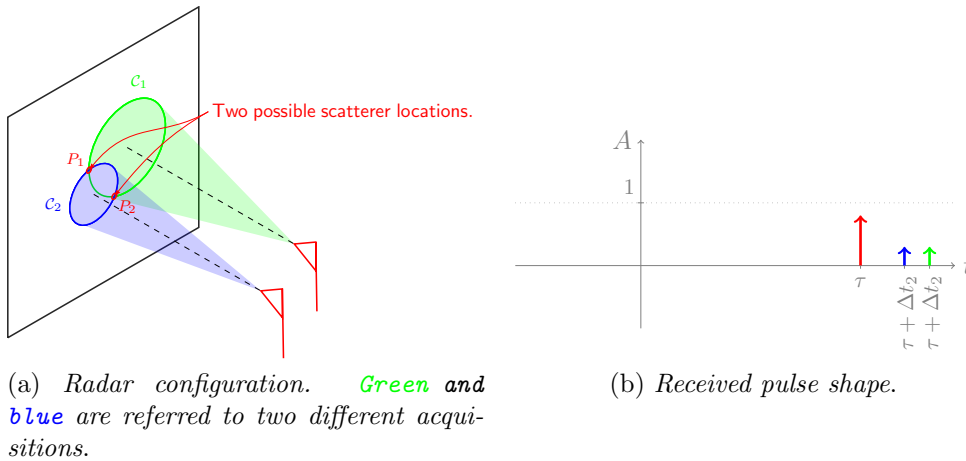


Figure 3.10: Defect location based on two observations.

mum of three non-concentric circumferences - and thus three non-coincident observation points - are necessary.

The particular case of the observation point right above the flaw usually causes a negligible variation of the response, since very small time delays are involved. However, exaggerating the delays, it can be treated distinguishing whether the flaw - assumed to be a *bulge* - is convex or concave. The former case represents an excess of material and let the signal to be reflected before than expected due to a distance which is lower than the one known *a priori*. This would results in the received waveform of Figure 3.11 which shows an

anticipation of the expected return pulse.

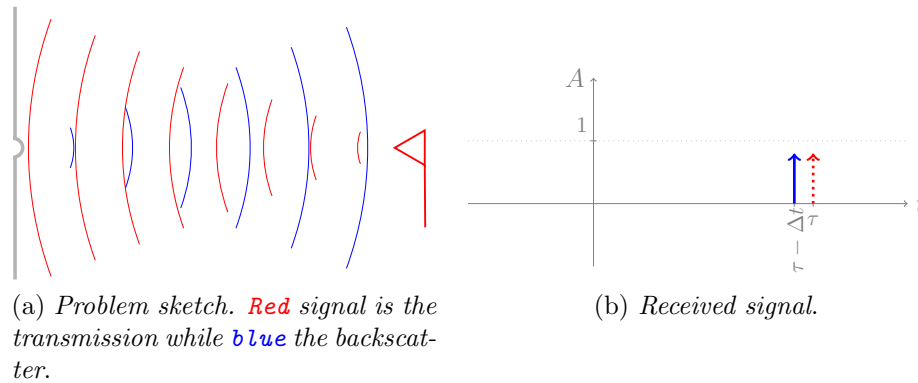


Figure 3.11: Convex bulge problem.

On the other hand, the latter case could be seen as a lack of material and in general causes some low shift of the pulse peak which is slightly delayed. By the way, to have a more realistic view of the problem, it should be accounted for the radar beam aperture which hits the corners of the concavity. Of course, the return signal still has the shape of the transmitted pulse and also the position will be approximately the same. However due to signal diffraction at the corner, the amount of the radiation scattered toward the radar and thus the acquired signal, will be very low (Figure 3.12). The result is much clearer in case of an hole, where the main peak may also disappear.

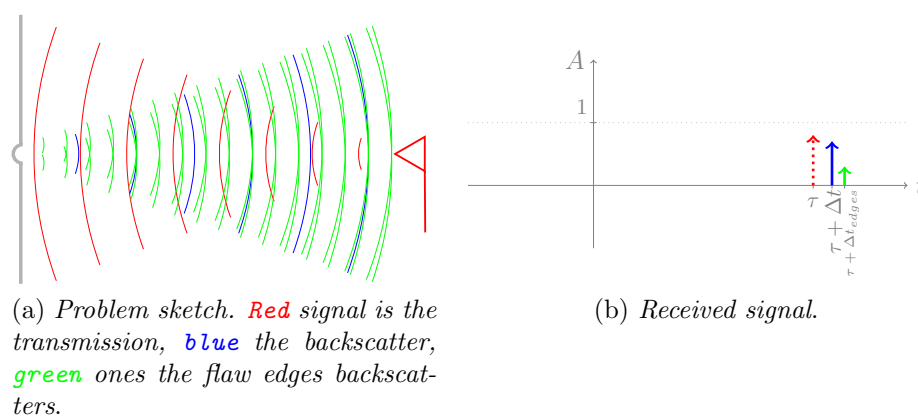


Figure 3.12: Concave bulge problem.

The idea of the SAR is basically an extension of what we have seen so

far. It consists in the observation of a static scene from multiple points. The obtained waveforms are then linearly combined to compute the image of the scene. This let us solve the scatterers' location issues, since multiple informations are given by several signals each one looking at the temporal point which corresponds to the flypath distance to the investigated point. In principle this method would allow to increase system accuracy and form images of the reflectivity. Applying it to a UWB radar should provide even a more consistent results due to the high information content provided by the large radar bandwidth.

In the following sections an algorithm is proposed to compute the images exploiting preprocessed waveforms provided by multiple observation points.

3.5.2 Imaging algorithm

The image representing the reflectivity of the scene can now be computed. The algorithm implemented is quite simple, although it would be completely ineffective if the above-described preprocessing is not performed to obtain time aligned waveforms.

Let now consider the three-dimensional matrix containing the waveform samples, obtained at the end of preprocessing routine and denoted by

$$S = s_{i,j}(kT_s) \quad i, j = 1 \dots 100, k = 0 \dots 255.$$

We are looking for a method which lets us combine the set of waveforms to generate an image from which is possible to identify a specific defect. An approach proposed in [22] consists of performing a time-coherent point-by-point superposition of the waveforms and eventually apply a weight to each contribution. The idea is that each pixel value is computed taking into account not only the corresponding azimuthal acquired waveform, but the whole set of waveforms, shifting each waveform observation sample, based on the additional flytime due to spatial separation of the points. To this purpose, denoting by I the image matrix, the generic pixel of the image is

computed as

$$I_{i,j} = \sum_{m=1}^{100} \sum_{n=1}^{100} w_{(m,n),(i,j)} \cdot s_{m,n}(k_0 T_s + k \Delta T_s) \quad i, j \in [1 \dots 100] \quad (3.3)$$

where

- $w_{(m,n),(i,j)}$ is a weight applied to the sample $s_{m,n}(k_0 T_s + k \Delta T_s)$ which decreases as the distance between the pair (m, n) and the pair (i, j) increases, according to a 2D Gaussian distribution;
- $s_{m,n}(k T_s)$ represents the discrete time signal acquired when the radar is azimuthally over the pixel (m, n) , which contributes to the considered pixel by a value provided by a time delay from the reference sample $(k \Delta T_s)$ computed based on trigonometrical considerations.

Although (3.3) considers the whole waveform set for each pixel computation, a slightly different procedure is adopted, where an image with reduced 50×50 size is formed but each image pixel value is computed based on a waveform submatrix with the same dimension 51×51 . Specifically:

$$I_{i,j} = \sum_{m=i-25}^{i+25} \sum_{n=j-25}^{j+25} w_{(m,n),(i,j)} \cdot s_{m,n}(k_0 T_s + k \Delta T_s) \quad i, j \in [26 \dots 75]. \quad (3.4)$$

Figure 3.13 shows that the surface on which the image is computed correspond to a smaller portion of the scanned area, and that a 51×51 waveforms matrix is used to compute each pixel value. On the other hand, if the image were computed on the whole scanned area, it would have provided a sort of dome, because an increasing number of points with higher weight are considered for central pixels.

3.5.3 Geometric considerations

In order to compute the sample to be considered in the waveform in position (m, n) , we need to compute the delay $k \Delta T_s$.

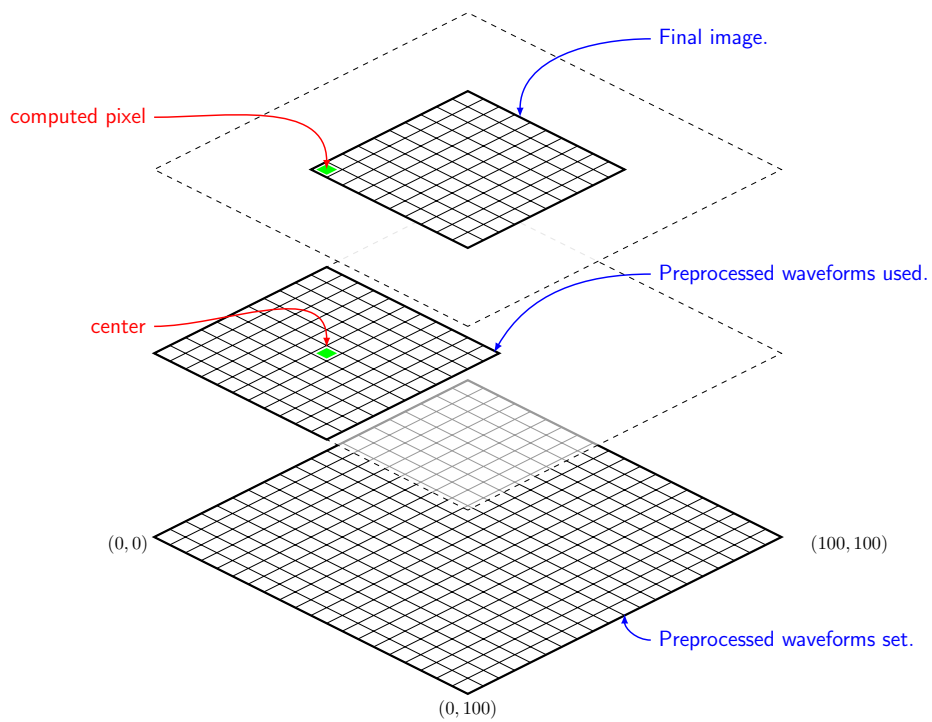


Figure 3.13: SAR imaging areas. Middle layer represents the set of 51×51 waveforms used to compute the value of the green pixel in the upper layer. The lower layer is the 100×100 matrix of acquired waveforms.

First of all, an important assumption has to be made about the dielectric lens mounted on the antennas. Since no experimental proof has been carried out, nor specific documentation has been accessed, it is neglected the effect on the propagation delay time i.e. it is assumed the flypath propagation delay due to the lens is equal in any direction. Although the effect of the dielectric is obviously to slow down the signal's speed, the overall result is not affected - under this condition - since we are interested only in time difference of two flypaths both passing through the lens.

Let us now consider the radar device centroid to be over the pixel (x_r, y_r) . If we are looking for the pixel (x_r, y_r) , the Time of Arrival (ToA) computation reduces to the determination of a length in a 2D symmetric problem as depicted in Figure 3.14. Thus,

$$ToA_{x_r, y_r} = \frac{2}{c} \sqrt{h^2 + \left(\frac{L}{2}\right)^2} \quad (3.5)$$

represents the minimum ToA among all the possible received echoes from the specimen.

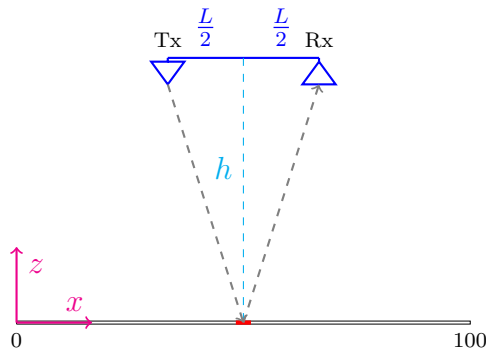


Figure 3.14: SAR: 2D geometric problem.

In contrast, in order to get the contribution to pixels out of the radar centroid, the time delay is computed solving the 3D geometric problem shown in Figure 3.15. Pythagorean theorem has to be applied twice, to solve the 3D triangles computation, one for each travel segment (Tx-to-pixel and pixel-to-

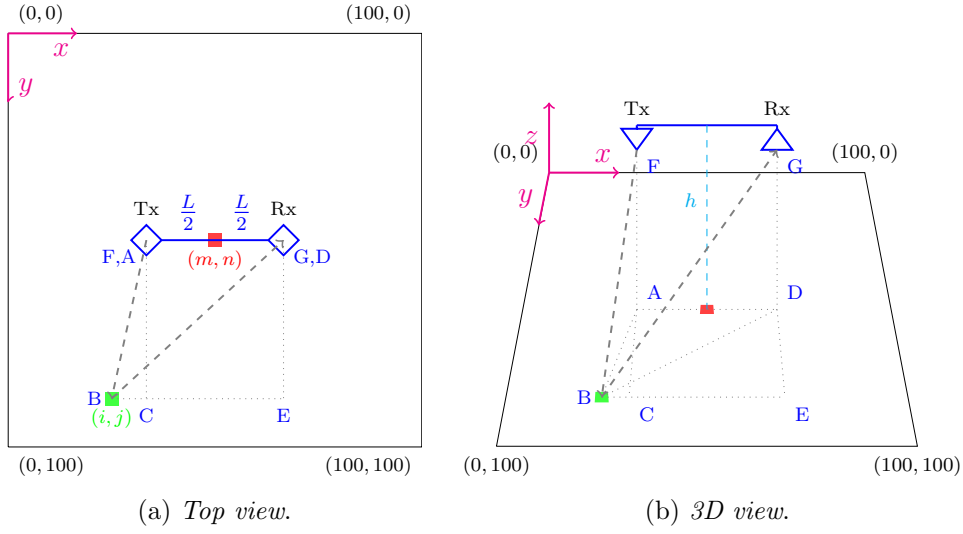


Figure 3.15: SAR: 3D geometric problem.

Rx). First, in top view (Figure 3.15a), the distance to the pixel is computed assuming the radar centroid in (x_r, y_r) and the considered pixel in (x_p, y_p) . Let us denote by (x_{rx}, y_{rx}) and (x_{tx}, y_{tx}) the coordinates of the two antennas, respectively. We have

$$\begin{aligned}
 y_{rx} &= y_{tx} = y_r; \\
 x_{rx} &= x_r + \frac{L}{2 \cdot \text{step}}; \\
 x_{tx} &= x_r - \frac{L}{2 \cdot \text{step}};
 \end{aligned}$$

where $\text{step} = 1 \text{ mm}$ is the step of radar scan. Since two different paths are formed from and to the radar, the computation is split in two paths, whose top view projections are provided by

$$\begin{aligned}
 \overline{AB} &= \sqrt{\overline{AC}^2 + \overline{BC}^2} = \sqrt{|y_p - y_{tx}|^2 + |x_p - x_{tx}|^2} \\
 \overline{BD} &= \sqrt{\overline{DE}^2 + \overline{BE}^2} = \sqrt{|y_p - y_{rx}|^2 + |x_p - x_{rx}|^2}.
 \end{aligned}$$

Move now to consider the 3D view in Figure 3.15b. Since A and D are the projections of Tx and Rx antennas on the plate, the 3D paths for Tx and Rx are

$$\begin{aligned}\overline{BF} &= \sqrt{\overline{AB}^2 + \overline{AF}^2} = \sqrt{\overline{AB}^2 + h^2} \\ \overline{BG} &= \sqrt{\overline{BD}^2 + \overline{DG}^2} = \sqrt{\overline{BD}^2 + h^2}\end{aligned}$$

respectively. The flightpath is finally the sum of these latter segments, i.e.,

$$\text{path}_{x_p, y_p} = \overline{BF} + \overline{BG}.$$

Thus, the signal travel time from radar to pixel and return is:

$$ToA_{x_p, y_p} = \frac{1}{c} \cdot \text{path}_{x_p, y_p}. \quad (3.6)$$

The extra travel time is obtained as difference of (3.6) and (3.5), namely,

$$\Delta ToA = ToA_{x_p, y_p} - ToA_{x_r, y_r}. \quad (3.7)$$

Since the waveforms are stored as samples, the value of ΔToA is mapped into sample waveform index, using the relation

$$\Delta S = \Delta ToA \cdot f_{\text{sampling}} \quad (3.8)$$

where f_{sampling} is the sampling rate. Now we may compute the sample delays from the reference, which is arbitrary taken to represent the acquisition performed when the radar centroid is azimuthally over the pixel. Calling S_{ref} the reference, the sample to consider for each other radar position with respect to the computing pixel is

$$S = S_{ref} + \|\Delta S\|$$

where the notation $\|\cdot\|$ is the rounding value to the closer integer.

An alternative to rounding ΔS is to provide a linear interpolation of the curve between the two points which are *floor* and *ceiling* of ΔS and eventually compute the value of the function in the exact point.

3.5.4 Weight matrix

During image pixel computation, a weighting factor is applied to the sample of each waveform, depending on the distance from the pixel position. Intuitively, waveforms acquired with radar closer to the considered pixel assure a higher accuracy due both to higher antenna gains and larger quantity of energy backscattered in radar direction, as the beam is quite orthogonal to the specimen. Instead, when the radar moves further from the pixel the backscattered energy becomes lower, since the incident angle is quite small.

Based on the radiation pattern of the antenna in Figure 2.4, a Gaussian weight has been chosen. Since we are dealing with a 2D problem, the weight function is built as a bidimensional distribution by the product of two orthogonal statistically independent Gaussian distributions. The obtained Probability Density Function (p.d.f.) is:

$$f_W(x, y) = \frac{1}{\sqrt{2\pi\sigma_x^2}} e^{-\frac{(x - \mu_x)^2}{2\sigma_x^2}} \cdot \frac{1}{\sqrt{2\pi\sigma_y^2}} e^{-\frac{(y - \mu_y)^2}{2\sigma_y^2}}$$

where μ and σ^2 represent, respectively, the mean and the variance of the distribution. Hence the 51×51 weight matrix W is built computing each cell p.d.f. considering the values of $(x - \mu_x)$ and $(y - \mu_y)$ to be the distances from the central cell (μ_x, μ_y) . This is because the weight matrix will be eventually used to compute each image pixel by setting this central cell on the pixel under the radar centroid. Moreover the variance is chosen such to match antenna specifications, which states a power content decay of 3 dB (50%) in a 40×35 degree cone. Thus a circular base cone approximation was chosen with radius

$$r_{3dB} = d_{specimen} \cdot \frac{\alpha}{2}$$

where $d_{specimen}$ is the specimen distance and α is the cone angular aperture. Although not strictly necessary to the computation, the total volume under the Gaussian is normalized to 1, to respect the definition of p.d.f.. The computed matrix is surfed in Figure 3.16. It is furthermore possible to verify that half of the weight matrix Cumulative Density Function (c.d.f.) for the area of the 3 dB cone is equal to 0.5.

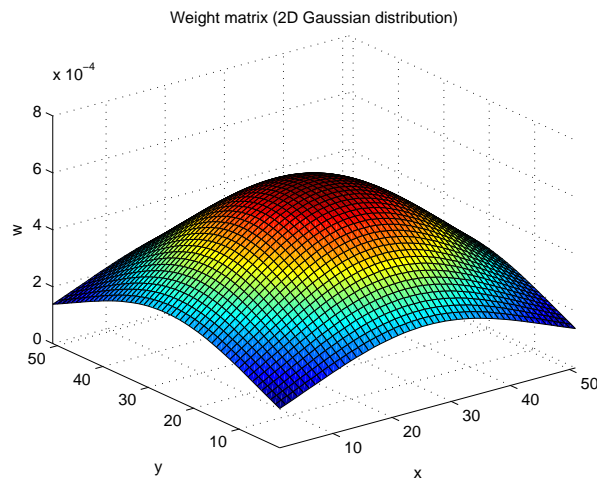


Figure 3.16: Weight matrix.

3.6 Defect detection

Consider now a new plate without any *a priori* information about the possible presence of any kind of defect. An automatic procedure is developed to scan the entire specimen and detect any flaw. Moreover, the algorithm also provides the comparison to a database set of sample defects previously collected, hence it is able to recognize if the defect occurring in the observed plate is still present in the database.

3.6.1 Plate scanning

In Section 3.3 the procedure for samples plate scanning has been exhaustively explained. Since the waveforms acquisition algorithm simply requires to record the radar received echoes in a $n \times m \times 256$ matrix, the values of n and m can be adjusted to let the device scan the area of interest. Furthermore both physical and theoretical restrictions should be considered when setting this parameters. The former are due to device motion end-points which bound the scanner to a maximum area of 300×250 mm. The theoretical limits, instead, are set to avoid borders effect, as largely stated before. Hence a satisfactory scanning area results to be 300×200 mm.

3.6.2 Data processing

Despite the fact that a larger amount of data should now be handled, also the processing algorithm basis remains the same as the one used for the samples computation. Nonetheless some important considerations have to be done:

- Some issues with RAM overflow may occur when using large amount of data (computing a 300×200 point scanning we ran out of memory³);
- It is important to be compliant with the samples acquisition, thus each pixel has to be computed using the same observable area used for the database samples, hence a 51×51 observation area is investigated for each pixel.

The first point can be easily solved either increasing the RAM capacity or removing the pure noise part (e.g., the samples with index less than 100) of the signal, before resampling the waveforms (in the case also the computing time is reduced). On the contrary the latter point is quite tricky. In fact, using an observation window as wide as half of the acquired image do not cause any error but it could lead to substantial different reconstructed images,

³Using a 16 GB RAM Windows 10 PC.

in particular if we are quite close to a defect. This should be prevented setting a fixed observation window which is applied to compute the reflectivity map.

3.6.3 Database comparison

Once the reflectivity map has been calculated, the software should provide a comparison with the samples already stored in a database. Since a likelihood measure of each kind of defect is required, the concept of *image similarity* is applied using the two-dimensional correlation. Although many different methods are available to provide template matching, only three were considered, namely *corr2*, *xcorr2* and *normxcorr2*. At the end of a brief investigation, *corr2* has been elected as the best candidate to achieve the template matching.

The embedded Matlab function *corr2*(I_{obs}, I_{db}) provides a scalar value from the comparison of two different matrices of the same size. Since the specimen image is usually much larger than the defect plate image, the software provides a comparison routine which does not return a single scalar value but compile an image of the correlation map pixel by pixel. Let us assume the database samples (I_{db}) are 50×50 pixels whilst the specimen plate⁴ (I_{coupon}) is 200×100 pixels. Thus the observation window (I_{obs}), i.e. the matrix size used to correlate with the defect sample, is 50×50 . The correlation map is generated using the concept of *sliding window* i.e. a mask of the same size of the template, which shifts at each iteration over the specimen image, from which the matrix I_{obs} is extrapolated (Figure 3.17).

Once introduced a suitable definition of the two matrices involved, a procedure should be given as well. In the following list all the steps of the correlation map computation are described starting from the availability of $I_{template}$ and $I_{specimen}$.

1. Initialize $col = 1, row = 1$;
2. Place the upper-left corner of the mask in (col, row) of $I_{specimen}$;

⁴Although 500×500 mm plates were used, the scanned area is 300×200 mm, smaller to avoid borders effects.

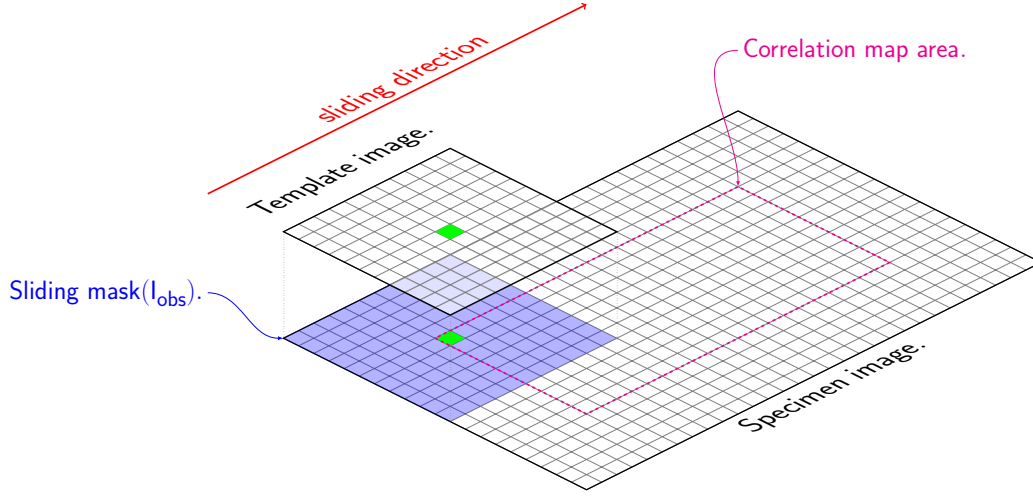


Figure 3.17: Sliding window for corr2 computation. The blue area represents the mask for I_{specimen} .

3. Compute I_{obs} by applying the mask to I_{specimen} ;
4. Compute the pixel $(\text{col}, \text{row}) = \text{corr2}(I_{\text{obs}}, I_{\text{db}})$, i.e.

$$I_{(\text{col}, \text{row})} = \frac{\sum_m \sum_n (A_{mn} - \bar{A})(B_{mn} - \bar{B})}{\sqrt{(\sum_m \sum_n (A_{mn} - \bar{A})^2) (\sum_m \sum_n (B_{mn} - \bar{B})^2)}} \quad (3.9)$$

where $A = I_{\text{obs}}$ and $B = I_{\text{db}}$, whilst $\bar{A} = \text{mean2}(A)$, $\bar{B} = \text{mean2}(B)$;

5. Slide the mask
 - (a) In general $\text{col} = \text{col} + 1$;
 - (b) If the mask has reached the limit of I_{specimen} columns thus restart to next row beginning $\text{col} = 1$, $\text{row} = \text{row} + 1$;
6. Loop from point 2 until the end of last row is reached;
7. Rotate the specimen clockwise of an angle equals to α degrees;
8. Loop from point 1 to 7 for any $\alpha \in \{0, \gamma, 2\gamma, \dots, k\gamma, \dots, 360 - \gamma\}$.

The above proposed procedure let the correlation map to be calculated for each of the database samples, in any orientation in the set $\{0, \gamma, 2\gamma, \dots,$

$k\gamma, \dots, 360 - \gamma$. During the test campaign, only four orientations were specified, namely $\{0, 90, 180, 270\}$.

Thus an image is computed for each database sample and the response depends both on distribution and amplitude of the correlation map. An area with higher values means the defect we are looking for is more likely to occur in that region. As a consequence we should observe a corresponding decreasing of the correlation with respect to healthy plate. On the contrary, if an area is likely to be undamaged, it would provide an increasing healthy plate correlation and a decreasing value for any other defect type.

To sum up, relevant information could be easily extrapolated from the sample correlation maps. First of all one may distinguish between damaged and healthy areas in a more significant way with respect to the observation of the reflectivity map. Furthermore the typology of defect, if present, could be highlighted by setting a threshold level for the maximum of defect-correlation map which also let the software to locate and isolate the damaged area.

3.7 Summary

What we have seen so far are the procedures used both for templates acquisition and specimen analysis. In particular the algorithm is quite similar, and differs only for the very last part of database comparison, as described in Section 3.6. For sake of clearance the algorithm is reported in form of flow chart in Figure 3.18.

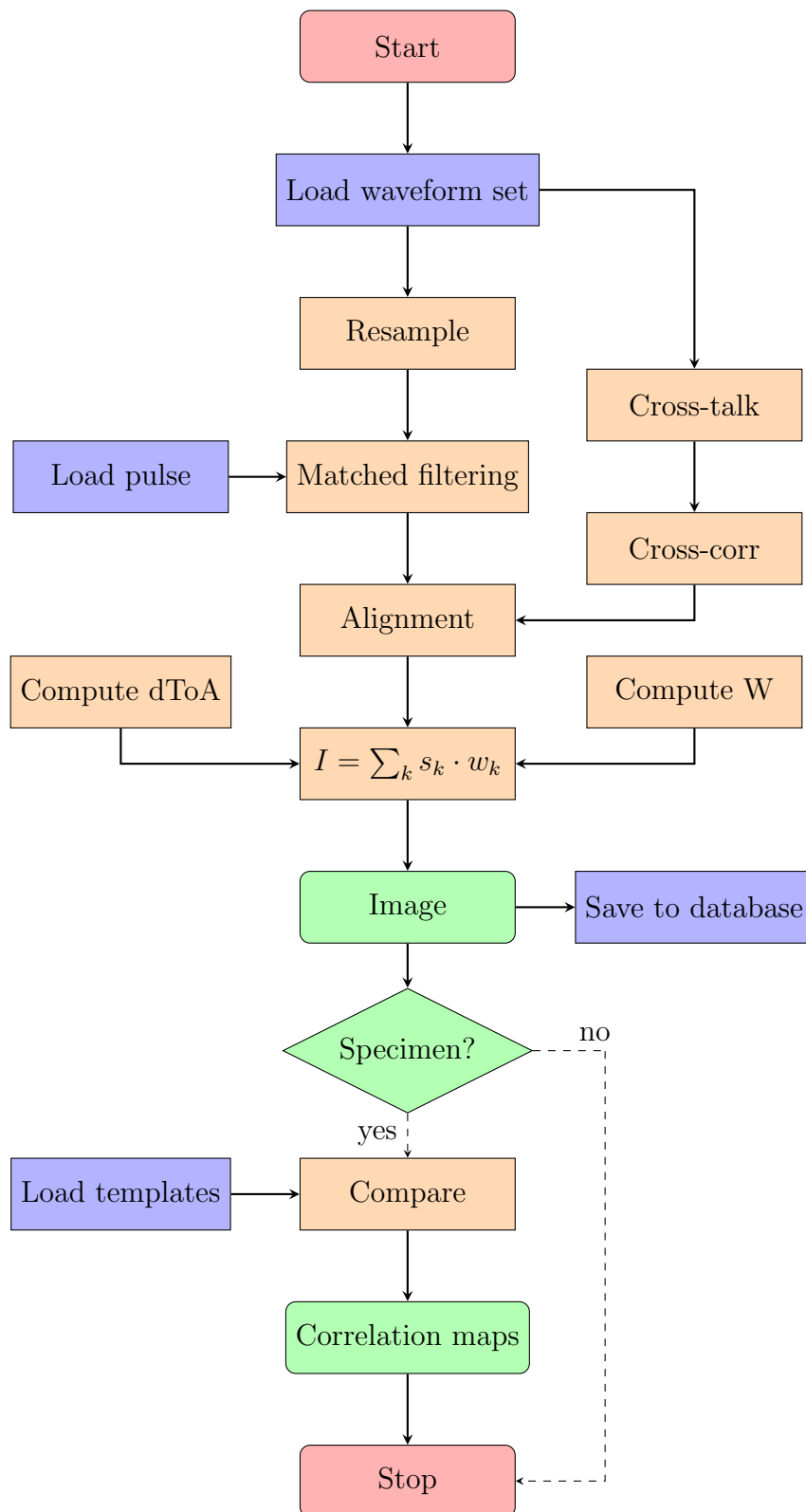


Figure 3.18: Process flowchart.

Chapter 4

Experimental results

4.1 Test campaign

The test campaign has been carried out in the Telecommunication laboratory (Cesena campus) at the School of Engineering and Architecture of the University of Bologna. The set up as well as the software parameters initialization have been described in the previous chapters. The obtained results are herein presented and commented. In principle the UWB-SAR method is applicable to EM reflective materials since the reflection as well as the material flaw-induced EM field depends on the plate reflectivity. The method results to be valid also on different types of material, such as carbon fiber, which shows properties of electrical conductivity capable to generate a proper response ([15]). Hence, two different materials have been used for the specimen, namely an aluminum plate and a carbon fiber plate obtained from pre-preg fabric.

4.2 Considerations

When observing the reflectivity images, one should focus on some critical points:

1. Pixel range values and maximum value;

2. Image pattern;
3. Visual similarity to the scene.

On these three points it worth spending some words before analyzing the algorithm outcomes. Considering the first point we should remind that the analyzed data are not generated from EM simulations, but come from real acquisitions. As such, the boundaries conditions (environmental noise, radar clock stability, motion device step precision, etc . . .) for each set of data, may affect the final results. Hence, pixel ranges of two images can be considered *equals* if they are of the same magnitude, irrespective for small variations in the result.

Concerning the second point something more should be said. As pixels values usually change with respect to the surrounding ones, some gradient may occurs in the formed image. Apart from the images representing defects, where the changes in reflectivity related to the defect causes a distinctive gradient, in case of undamaged plate the image pattern is not so clear. This may be due to several conditions, such as plate misalignment with respect to the radar scanning plane, inducing a side-to-side gradient, or an incorrect position of the radar antennas, whose reciprocal position could be slightly modified by motion device accelerations. Fortunately, the resulting gradient is usually quite small in magnitude such that it does not compromise the image recognition. A further cause which may affect the pattern is the presence of people in the testing room, in particular those accessing the area of the specimen background. Since 50% of the antenna radiation is spread in a 35×40 degree cone, each target inside this area, if reasonably close to the radiation source, cannot be a priori distinguished from the static background. In addition the acquisitions were quite long and the laboratory access could not be prevented, hence some minor pattern variations in images may be visible.

Finally one should not thinks that the reflectivity image is an exact picture of the visual pattern of the scene, as it represents the behavior of the EM fields in the area of interest. In order to know a priori what to expect, a

study of the EM field should be done based on material specifications, surface and boundary conditions as well as the defect shape [22]. In addition to those considerations, two further conditions may affect the final result, namely the distance focusing and some other general issues which are deeply described in the following two subsections.

4.2.1 Distance focusing

The distance between the radar and the specimen is assumed to be known. Nevertheless, it is a mere measurement of the separation between the plane of the antennas' radiative element and the coupon surface. Since this distance is translated inside the algorithm in a light time distance (i.e. a time delay), it may be affected by several error sources, above all the presence of the dielectric lens. For this reason, in a preliminary stage of this thesis some experimental testing has been carried out to provide a demonstration of the best selection for the observation starting point, i.e. the time instant of the waveform to be assumed as corresponding to the plate surface.

An investigation has been carried out on some macroscopic defect acquisitions, which were processed using the algorithm described in Section 3.5. In addition, several images were generated starting from each set of acquired waveforms, but setting different values both for coupon distance and signal's sample used as reference. From the so-obtained images (which are not herein presented due to space issues) we may conclude that the closer we are to the received signal's peak, the more the image is clear and the defect reconstruction is nicely visible. However, moving the *reference plane*, namely the observation distance at which the image is formed, strongly affects the visibility capability. Since the coordinates of the reference plane are defined in terms of starting sample (i.e. the one referring to perpendicular pixel observation, or minimum ToA), this could be shifted toward higher or lower values with respect to the maximum peak position. As a consequence, two scenarios are possible, which are depicted in Figure 4.1 for sake of clearance.

- If reference time is anticipated, i.e. the considered plane is moved

closer to the radar source, some defocussing has been observed and the image eventually represents nothing (healthy sheet) when the time anticipation reached the definition of a plane far from the plate more than the EM induced modification.

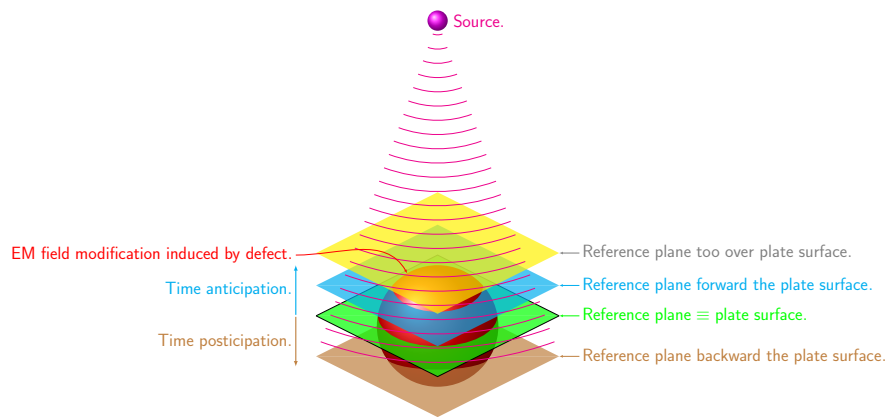
- If the time is delayed, i.e. the reference plane is moved behind the plate surface, the performances decay as well, even though in a different way. In fact considering a delayed samples on the signal means looking in the reflected pulse tail, which still contains some informations about the plate.

Although the experiment highlights the most suitable sample to be considered as reference is the reflection's maximum peak, some words could be spend to visualize the problem concept in a more theoretical framework. In fact, if a different frequency is set for the radar, which allow some material penetration capability, the trick of shifting the observation *reference plane* could be quite useful to obtain a sort of Computed Tomography (CT), thus informations about the internal status of the plate, and eventually detect other defects such as delaminations, flaws, etc... Of course, as suggested in [15], this should be integrated within a system which modulate the operative frequency, letting the signal to have a deeper penetration in the material, based on the model of power decay for that material.

4.2.2 Gaussian weighting tradeoff

Although in subsection 3.5.4 the parameters of the Gaussian weighting matrix are said to be in accordance to the energy distribution inside the antennas radiation cone, this does not agree to what is really implemented. In fact the first approach was to concentrate 50% of the Gaussian energy in a 35×40 degrees cone did not always provide the desired result.

First of all, let us introduce the formula for the Gaussian variance com-



(a) 3D view.

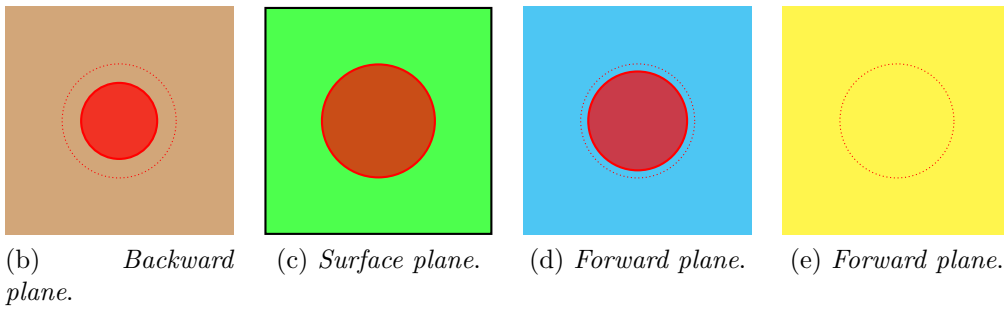


Figure 4.1: Effects of reference plane shifting. In **red** the trace of EM defect-induced anomaly is shown, whilst dashed line represents the trace on the surface plane (the **green** one).

putation for one axis (e.g. x-axis):

$$\sigma_x^2 = d \cdot \tan\left(\frac{\theta_x}{2}\right) \cdot k_{var} \quad (4.1)$$

where d is the radar-coupon distance, θ_x the radiation pattern cone aperture in the x-direction, namely the horizontal one, and k_{var} a corrective factor experimentally found close to 5.7 to have the correct Gaussian shape. What has been noticed is that the values of θ_x and θ_y are of great importance to the final result. Using high values of cone aperture, thus a large Gaussian bell, the image pixels are smoother since each position strongly contributes to the surrounding pixels computation. On the contrary, decreasing cone aperture angles lead each position loose its influence to the nearby pixels thus the obtained image will be more speckled as those values decrease. In extreme cases, the use of too large angle values may lead to the cancellation of important informations, possibly due also to some *fake acquisitions*, i.e. some non-consistent response waveforms acquired, for instance when a disturbance source was acting. An analysis of different effects of cone aperture is now reported for the *Specimen M2* which will be eventually presented in Subsection 4.4.1.

The specimen is a metal plate with a central drilled 5 mm diameter hole. The reason this coupon has been chosen to present Gaussian variance effects, is clear from Figure 4.2. In fact, it is easy to notice how the weighting may influence the formation of the reflectivity scene, with the possibility of jeopardize the final result, preventing small defects to appear due to figure smoothing. In particular this occurs in Figures 4.2d and 4.2e where the central pattern induced by the hole, visible using smaller Gaussian variances, is completely overlay by a stronger gradient pattern related to the boundaries of the image.

As a matter of fact, this issue has been observed only on specimen images based on waveform sets larger than the 100×100 template one. In order to be clear and let anyone to replicate this work results (which however strongly

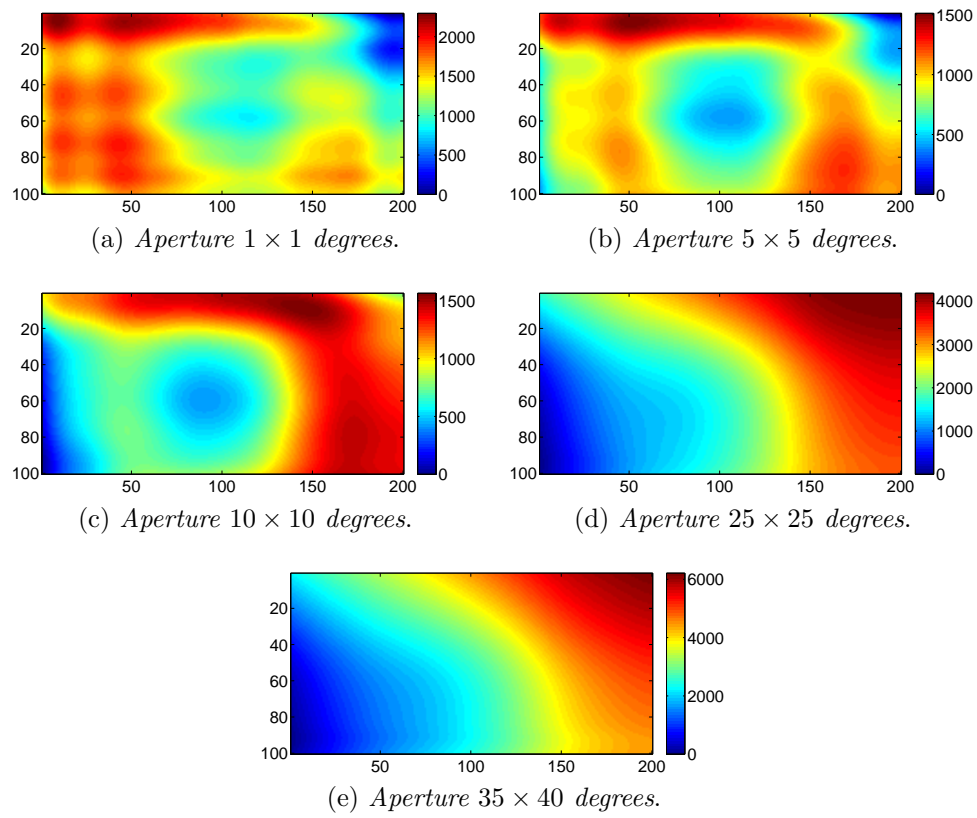


Figure 4.2: Specimen M2 reconstructed images at different Gaussian variance.

depends on acquisition boundary conditions), the antennas aperture cone applied in the computation is specified for each generated image.

4.2.3 General issues

The issues affecting the systems regards disturbances coming from different sources.

Although the human movements in the same room of the acquisition does not appear to cause any variation in the observables, this is not true if some operations occur near to the specimen¹. This is because they cause a variation in the background scatterers which are required to be constant and static.

No further important issues has been faced during the test campaign.

4.3 Database samples

All the SAR-image database samples below are 50×50 pixels representing the reflectivity map of a larger plate. The scanned area of 100×100 mm required a plate at least 100 mm larger for each side, to avoid border effects.

Before starting with the data presentation, we provide the concepts of Point of Interest (POI) and Region of Interest (ROI), useful to the reader for a better understanding of the associated discussions. POI denotes a particular feature of an image, such as a point or a shape. Instead, with ROI we indicate a cluster of POIs, also different one from the other, which are linked to a common cause. For instance, ROI is usually used to denote a defect image template, which consists of a well defined set of POIs through which it is possible to discern that image from any other one.

¹A similar problem has been faced if either air-conditioner runs or some air flows in the room (e.g. window-door). Since the coupon is only clamped at its lower border, and the sheet is very thin and light, the flux turn out to let the specimen vibrate, such to cause an inconsistent measurement set. Of course, such a problem would not occur in a possible application where the part is fixed to a more stable and heavier structure.

4.3.1 Metal plate

The idea at the beginning of this thesis was to demonstrate the method applicability on some composite specimens. However, a first study has been carried out on a metallic specimen, namely an aluminum 1 mm thickness plate of size 400×500 mm, with *C* shaped borders, as depicted in Figure 4.3. This sheet has been used to provide an extension of the set of the materials

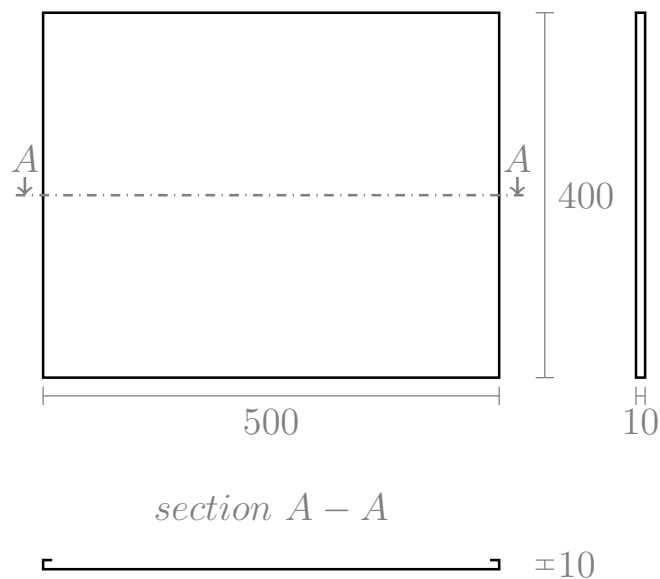


Figure 4.3: Metal plate draw.

on which the method is tested. In principle, on a metallic plate the detection should be easier, due to higher EM reflectivity which eventually highlights in a better way any field variation.

In the following, different type of defects have been considered and the reconstructed images are presented and commented.

Healthy

The first plate analyzed is an healthy one, without any added defect, as shown in Figure 4.4. The acquisitions were repeated twice to be sure a similar image could be obtained.



Figure 4.4: Metal healthy plate.

Even though a completely flat surface was expected, some gradient is visible in both image of Figure 4.5. As we already anticipated, this could

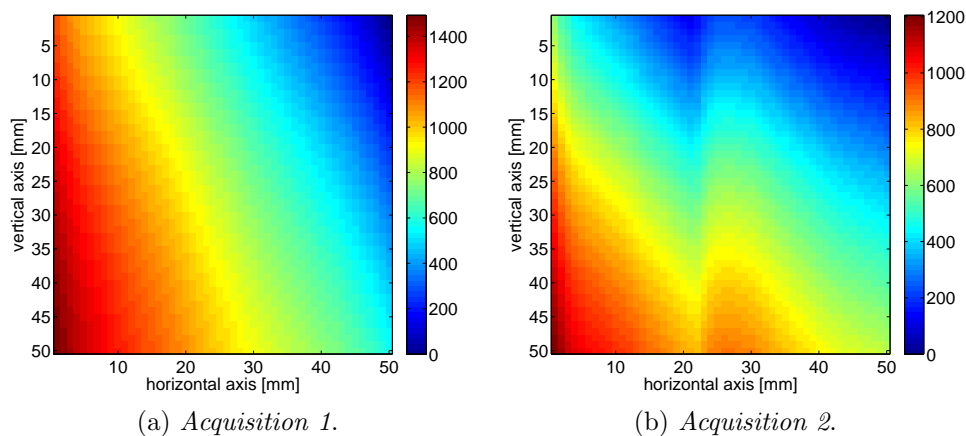


Figure 4.5: Metal healthy plate reconstructed image ($\theta_x = 35^\circ, \theta_y = 40^\circ$).

be explained by an imperfect alignment with respect to the radar scanning plane. In fact the radar support system is not properly designed such to be rigidly connected to the motion device, furthermore the non-infinite stiffness of the material may inducing some convexity of the plate clamped by a vice. In principle, a perfect knowledge of the distance of the plate using a Distance

Measurement System (DMS) for instance a laser device, may compensate for the misalignment and cancel out this effect, or at least enhance the image. On the other hand both images are visually similar, any variation, since reasonably small, could be charged to external disturbance sources. It is also possible to notice that the pixels amplitude ranges are similar between the two images, having their maxima between 1200 and 1500. As we will see later on, this range is much lower than any other defect image, thus it could be concluded it is almost negligible.

Central bulge

The second specimen acquired is a damaged plate with a central bulge of dimensions 8×8 mm shown in Figure 4.6. This specimen is obtained applying

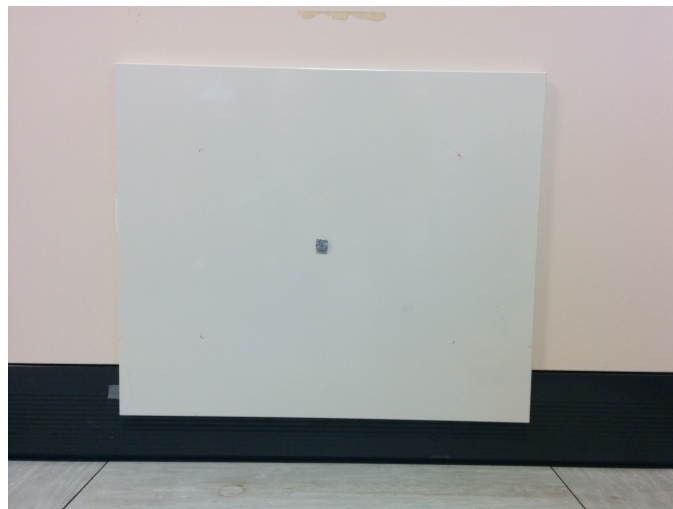


Figure 4.6: Metal plate with central bulge.

on the healthy plate an aluminum sheet folded on itself. The obtained images for two different acquisition are shown in Figure 4.7.

Both the images nicely show the central defect identified by a much higher value of the pixels. In fact, the value of the pixels has its maximum above 7000, thus is pretty easy to distinguish it from the healthy coupon. Also

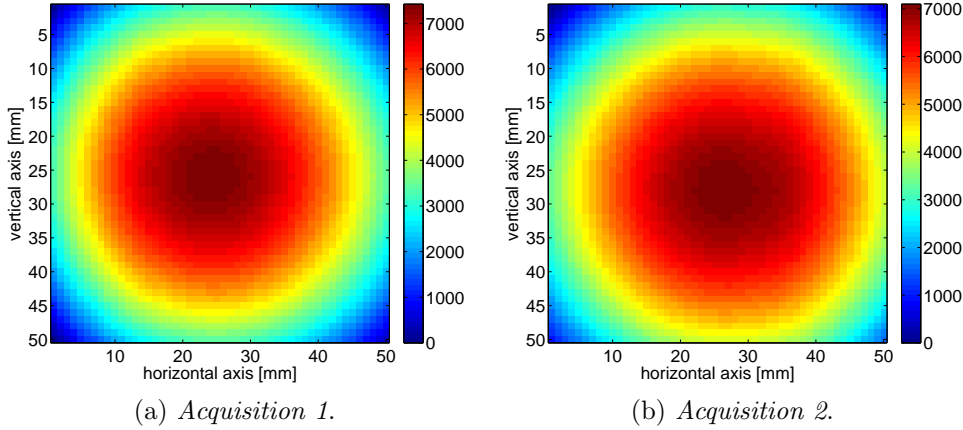


Figure 4.7: Metal plate with central bulge reconstructed image ($\theta_x = 35^\circ, \theta_y = 40^\circ$).

the pattern structure about the defect area is as expected. In fact the non-punctual beamwidth also collect informations from the non-azimuthal position, which eventually affects also the value of the maximum peak of the signal. This also yields the creation of a concentric circumferences pattern, where the pixels' values decay as the position in the image move far away from the defect. Of course, the decreasing in value is related to the increasing distance from the defect, which lets the waveforms far from the flaw be less aware to it.

In this case, the reflectivity map gives a precise idea of the visual image, since the central bulge is highlight by the dark red color. However, the physical bulge dimension is not easy to compute. In fact it should rely on a very accurate calibration, which at the end lets us know how much of the pixel value's range percentage has to be considered as the defect itself. Although in this case the darkest shade of red is about of the same size of the real defect, this is only a chance. This area depends on several physical and numerical parameters, first of all the colormap bit deepness. The colormap here used for the generation of the images is a *jet colors 256 bits*. If we had used, for instance, a 64 bits map of the same type, with the same resulting data, we would have obtained a much larger darkest red area. Thus the

reader should pay attention to the map, which only returns an *idea* of the effective behaviour of the EM field variation - and possibly of the real visual image.

Central hole

Another considered defect is represented by a circular hole. The metal plate previously used as the healthy reference, has been drilled with a diameter of 5 mm.

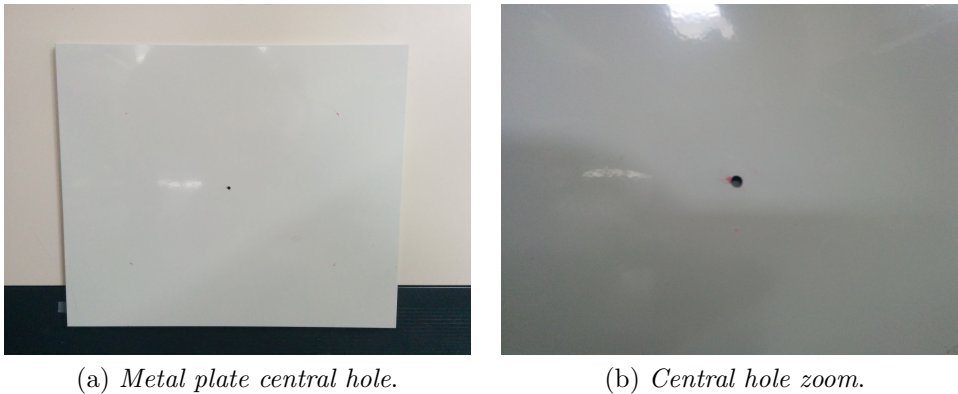


Figure 4.8: Metal plate with central hole.

Although Figure 4.8 shows a 5 mm drilled plate, smaller hole diameters have been investigated, but they do not provide any significant results. In fact, even though the difference between damaged and healthy plate is felt in terms of pixel range, the algorithm is not capable to correctly reconstruct any image of the defect. It is not clear if it depends on a too small defect size with respect to the radar resolution or a pattern superposition. In fact, also small misalignments are felt by the SAR and it may happen that the weak defect-induced pattern is superposed to a stronger one which hides it. However, a 5 mm hole is the smallest tested defect whose image reconstruction has been achieved, as shown in Figure 4.9. This defect is clearly visible and, as expected, is represented by a pixel low value area. Although, in a central bulge the POI coincident with the center of the defect is a peak of

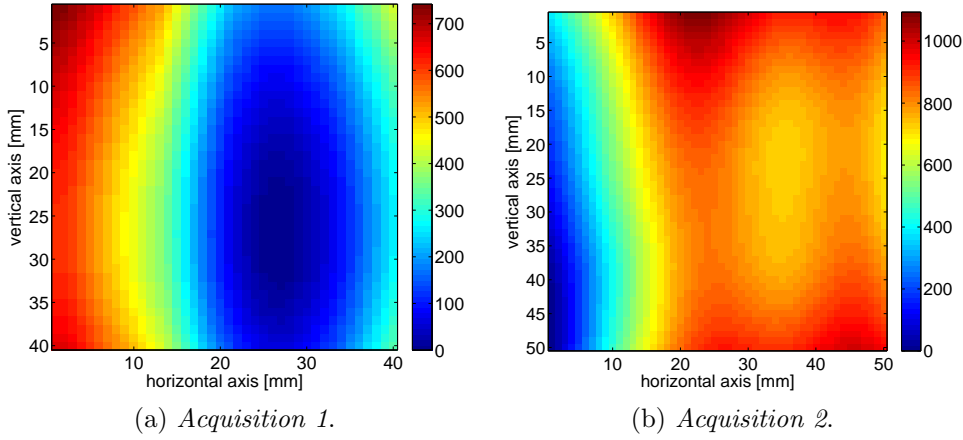


Figure 4.9: Metal plate with central hole reconstructed image ($\theta_x = 35^\circ, \theta_y = 40^\circ$).

amplitude much larger than the healthy maximum value. The most likely explanation is that the lack of material in the central region causes a much lower reflection and this area acts as a sink. Thanks to that, the hole ROI image is characterized by the hole providing a decreasing pixel values, whilst in the remaining area the undamaged plate value is basically maintained untouched.

On the other hand the image is quite squeezed along the horizontal direction. A possible cause for that is the antennas polarization interaction with the specimen induced EM field, since the polarization has a privileged direction, which means the problem is not isotropic. This, of course, is a possibility one may suggest and which should be confirmed by further EM studies.

4.3.2 Composite plate

The specimen has been manufactured in Material Structure Technology Research Laboratory (MaSTeR Lab) in Forlì. The plate has been obtained using 5 layers of carbon fiber pre-preg fabric, namely 200 gr/m^2 and thus of thickness 0.2 mm/ply . Finally, total plate thickness is about 1 mm .

As we did for metal plates, once the composite sheets were available the acquisition were performed both on healthy and damaged coupons and are described in the following.

Healthy

The first observation of the composite coupon has been performed on the healthy plate, without any intentional defect. Looking at Figure 4.10 several observations may be pointed out. Since the pattern is very similar in each

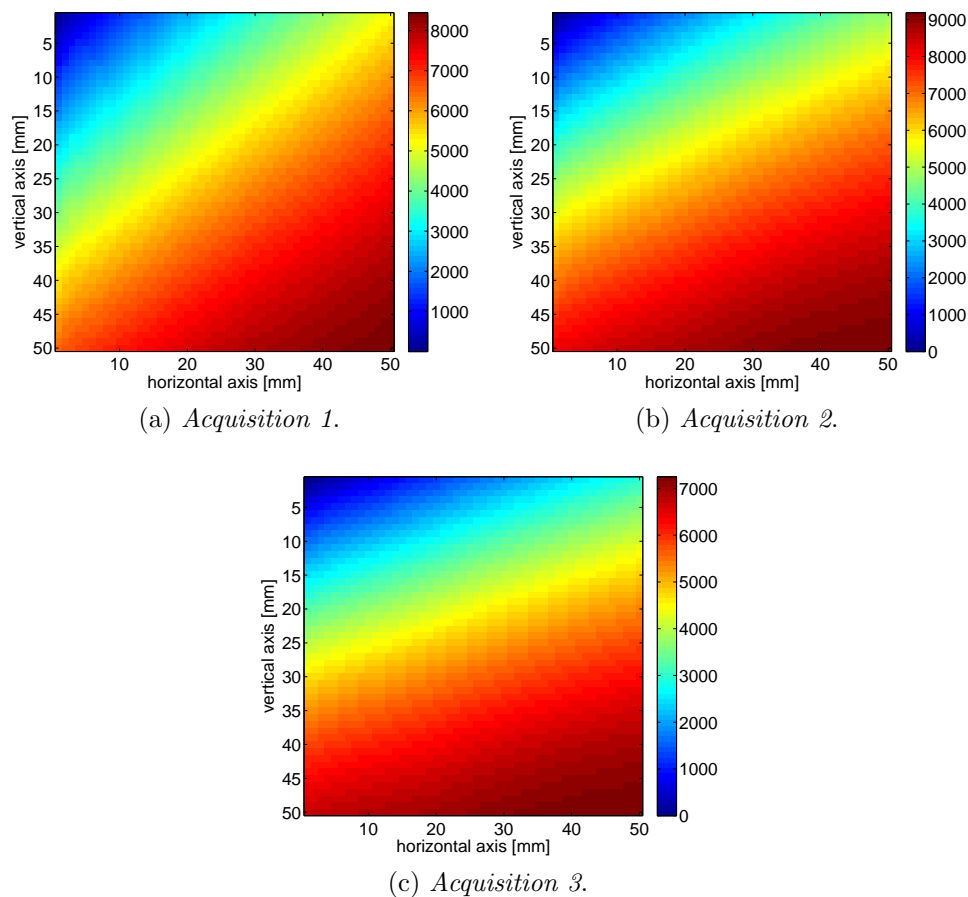


Figure 4.10: Composite healthy plate reconstructed image ($\theta_x = 35^\circ, \theta_y = 40^\circ$).

image, it represents quite an important result proving the repeatability of

the method. Furthermore the acquisitions, show the same range of values between 7000 and 9000. Similarly to the healthy metal case, gradient pattern images were obtained. The possible origins of the gradient have already been accessed, although it worth noting that no defect is visible.

Central hole

The first observed defect for the composite plate is the hole. Diameters lower than 5 mm did not provide clear results, even though the healthy pattern changed modifying the gradient in correspondence of the defect. The hole drilled in the composite plate is shown in Figure 4.11. Although in metal

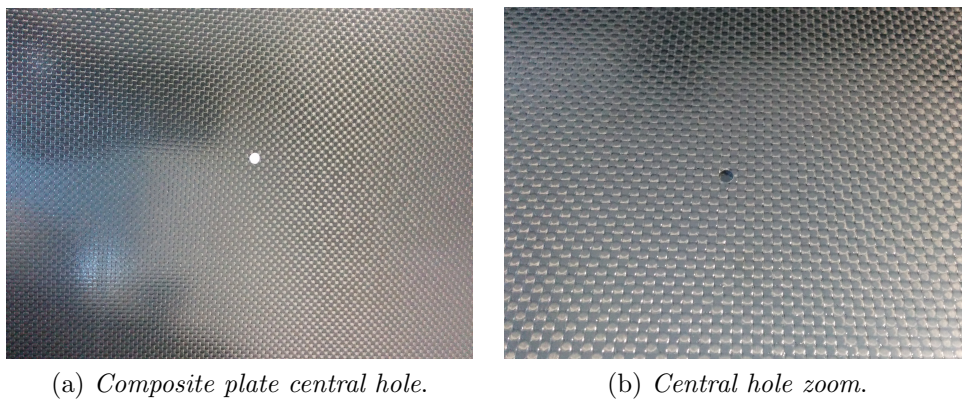


Figure 4.11: Composite plate with central hole.

coupon the hole is very clear in the reconstructed image, the acquisition boundary conditions make the composite image substantially different. First of all, because of the low thickness, the plate did not stand straight when clamped. Hence, it has been necessary to fix it to a plane support, such as the furniture wall of the laboratory. Although this does not cause any appreciable effect in the healthy plate, for the drilled one it causes the hole to be blocked up by the presence of such support. This caused different reflectivity properties. Observing Figure 4.12 one may notice that the hole position appears to be more reflective, in contrast with what was expected of a lower (or almost null) reflected power. However, this could be easily

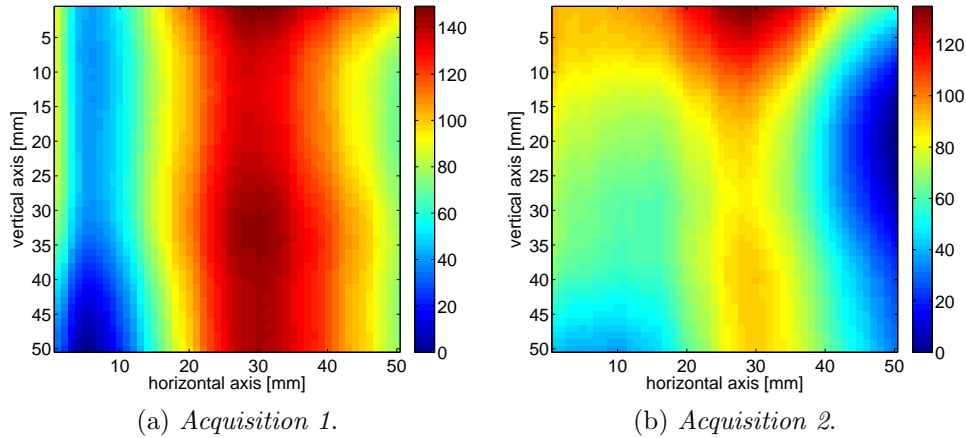


Figure 4.12: Composite plate with central hole reconstructed image ($\theta_x = 35^\circ$, $\theta_y = 40^\circ$).

explained considering the different flypath of the signal. The portion of the signal reaching the plate, propagates through the resin before being reflected back by the carbon fibers and being received, after a second passage through the whole resin layer. Instead, the components coming to the hole are simply reflected by the backward wall. Considering the resin effect, the signal not coming into the hole experiences a supplementary attenuation, thus a loss of signal power. Compared to the higher power reflected back by the furniture wall inside the hole, the defect becomes visible. The pixel's range is almost the same as well for the two images, being in between 130 and 150.

Above all, it should be remarked the importance of that discover: we are not interested in seeing purely the image reflectivity, but the difference of reflectivity between the undamaged part of the coupon and the background. This could be useful to analyze particular material by exploiting some tricks, such to observe a fiberglass specimen by wetting the fibers which, absorbing the humidity, could highlight the different reflectivity conditions in case of a flaw.

Unfortunately, as opposed to the metal template samples, it is easy to notice that the 50×50 pixels reflectivity map acquired as template in Figure 4.12 do not represent the drilled hole samples only, but the characteristic

ROI surrounded by a superposed plate pattern, thus the image should be cropped. Noting that the central area of the images represent the hole, it is possible to isolate and extract a 30×30 pixels ROI from each acquired sample. Therefore, the reduced size template samples are reported in Figure 4.13.

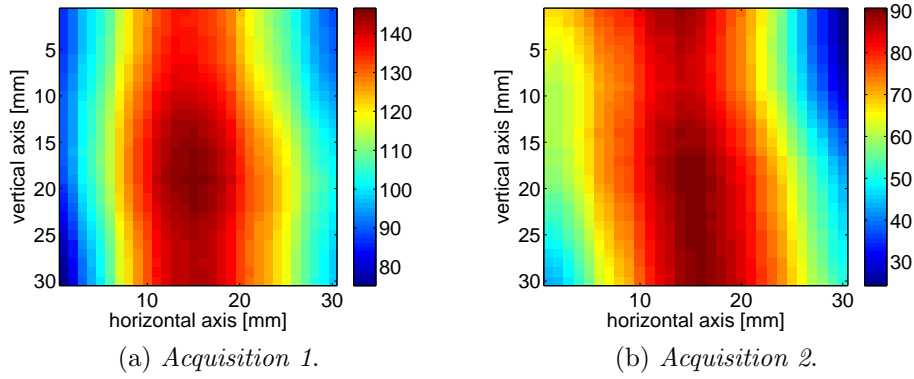


Figure 4.13: Composite plate with central hole cropped samples ($\theta_x = 35^\circ, \theta_y = 40^\circ$).

4.4 Specimens

So far, a suitable database of defect samples has been compiled. Thus we may now move to the detection of a flaw in a specimen without any a priori information. In order to save time and money, the tested plates were the ones previously used for templates acquisition, so we are looking for a defect recognition with exactly one of the acquired sample. The specimen waveforms were acquired and processed similarly to the template ones as described in Section 3.6. Once again, this section is divided into two parts, one for each tested material.

Due to the given limitations for border effects and the ones provided by the motion device, a 300×200 steps scansion has been performed using 1 mm step size.

4.4.1 Metal plate

The metal full-plate acquisitions were performed on two different damaged plates, whose defects are represented by the bulge and the hole respectively. Since neither the defects presence nor their possible shape and position are assumed to be known, these two plates are called *Specimen M1* and *M2* respectively.

Specimen M1

The following description is referred to defect recognition of the bulge defect visible in Figure 4.6. Before the scanning, the radar has been positioned such to have the bulge in the center of the observation window, so that Figure 4.14 was computed.

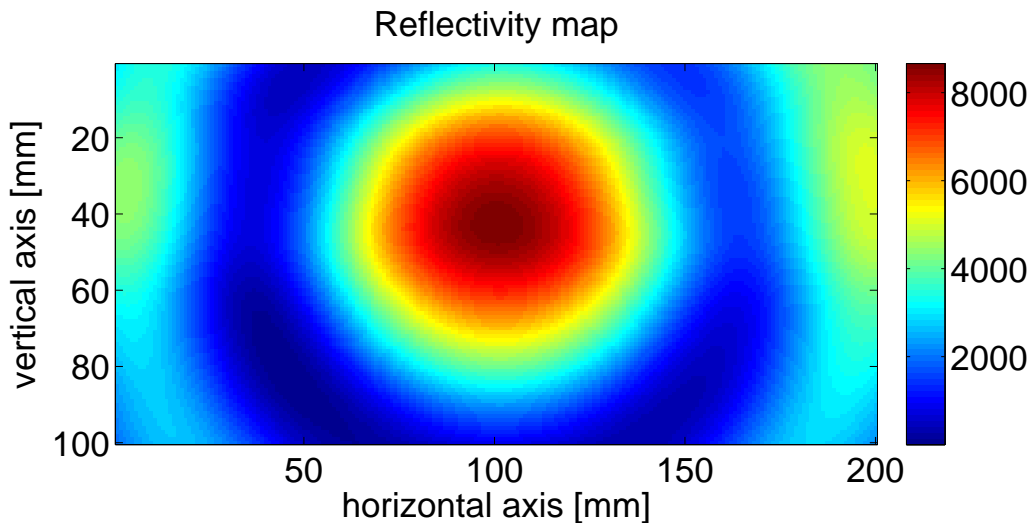


Figure 4.14: *Specimen M1* reconstructed image ($\theta_x = \theta_y = 10^\circ$).

As a matter of fact, it is clearly visible the central ROI gradient having the typical features of the bulge defect. Moreover it is verified that the scale range is about the same order of magnitude of the one provided by that defect template. Of course, this is what an operator - even untrained - can see.

Since the software aim is to be completely autonomous, the image has been automatically compared to each of the metal defect templates. The obtained correlation maps are provided by Figure 4.15 for each template sample and orientation in the set $\{0, 90, 180, 270\}$ degree. Each correlation map shows the areas with the best matching to the template applied in a given direction. To the algorithm is much more important the maximum correlation

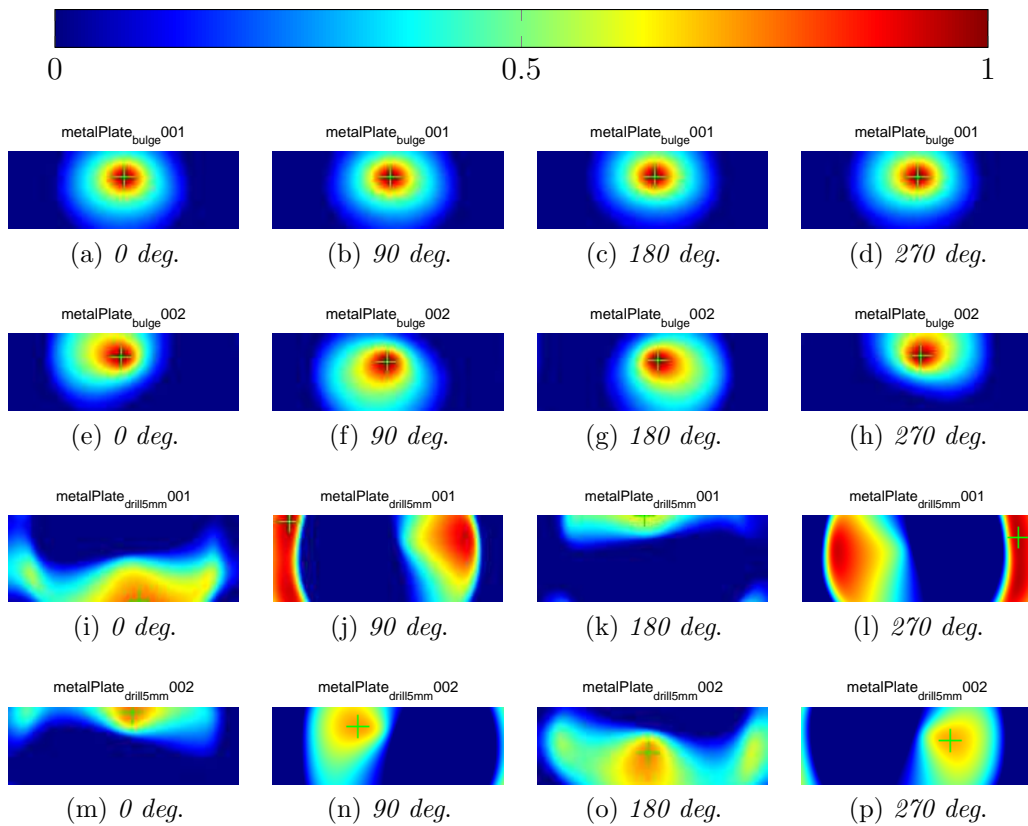


Figure 4.15: Specimen M1 correlation maps.

value obtained for each template, and its position. For this reason, Table 4.1 is filled with correlation peaks values and their coordinates expressed on the reconstructed reflectivity image. In this way, it is much programmatically easier to determine the presence of a defect - and contextually its kind - simply by comparing table values to a threshold. In this case, both the templates representing the bulge defect show correlation peaks of 99% in the

Table 4.1: Specimen M1 - templates correlation peaks.

Template	0 degree		90 degree		180 degree		270 degree	
	max	coord	max	coord	max	coord	max	coord
<i>bulge001</i>	0.99	101,42	0.99	102,42	0.99	102,42	0.99	101,42
<i>bulge002</i>	0.99	99,41	0.99	100,44	0.99	104,43	0.99	103,40
<i>drill5mm001</i>	0.77	116,85	0.95	37,30	0.63	100,26	0.95	176,41
<i>drill5mm002</i>	0.76	106,29	0.72	81,38	0.75	98,55	0.71	122,47

neighborhood of (101, 42). This is very close to the location where the defect were placed - or at least where it is intended to be - in the middle of the scan area. It should be concluded that the identification and positioning of the defect have been correctly detected (in Figure 4.16 the best matching template is located into the complete specimen image).

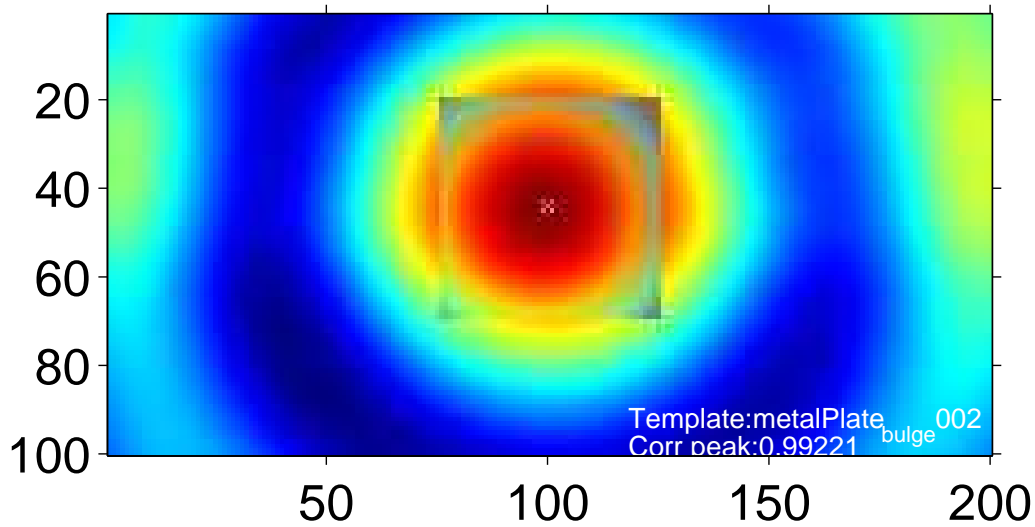


Figure 4.16: Specimen M1 template positioning.

On the other hand, the identification of the defect kind results to be successful as well, with a match of 99% to bulge defect type, whilst the correlation peaks remain below 95% in any other case, being about 70% in most of them. The high values found in two orientation for the *metalPlate_drill5mm001* to be so high, may obviously lead the system false alarm if a lower value of threshold for template match is set. For instance, excluding that two re-

sults, a reasonably threshold value would have been 85% matching to claim a template defect to be found. Obviously, since those values are found for a single template (not for both hole templates), and considering the occurring real defect, it could be said that the false alarm could be handled using a database compiled for more than one image sample for any defect template. Based on statistical considerations, instead of simple peak values, which have been found for the hole templates at 90 and 270 degree orientation, an overall mean is used to match any template orientation. This is computed to be 83.5% and 83% respectively, thus lower than the proposed threshold. This kind of issue may occur due to the very elementary defect shapes which could resemble some pattern induced by other causes. However, looking for more complex and articulated flaw shapes could improve this threshold gap as well.

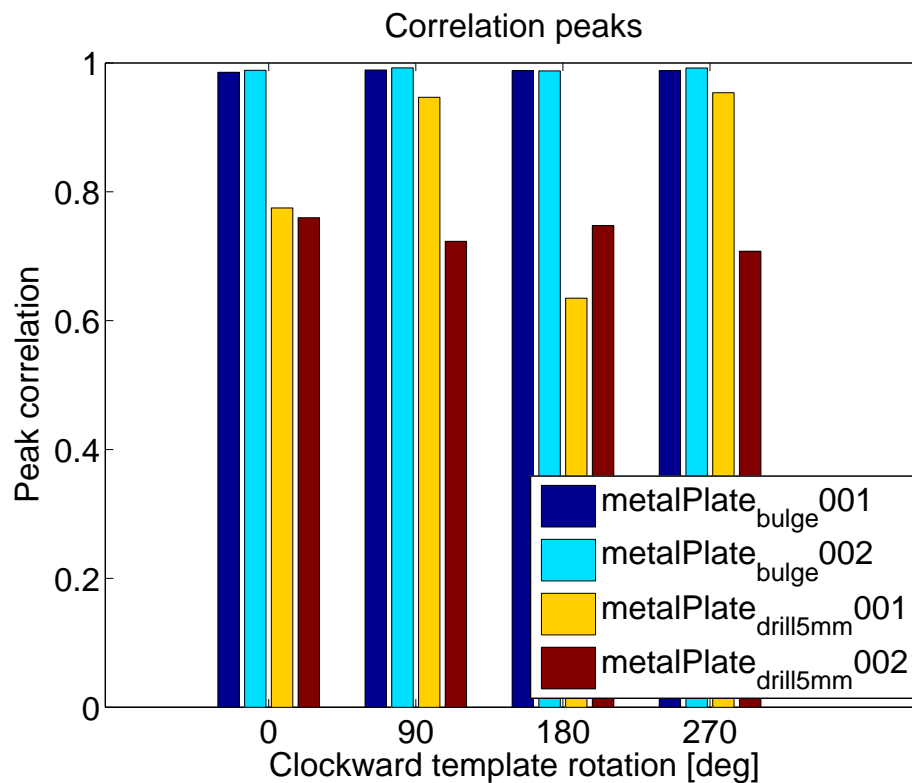


Figure 4.17: Specimen M1 correlation maxima.

For sake of clearance, a plot of the correlation maxima positions is also

reported in Figure 4.18 to let the reader figure out the best matching location for each of the templates.

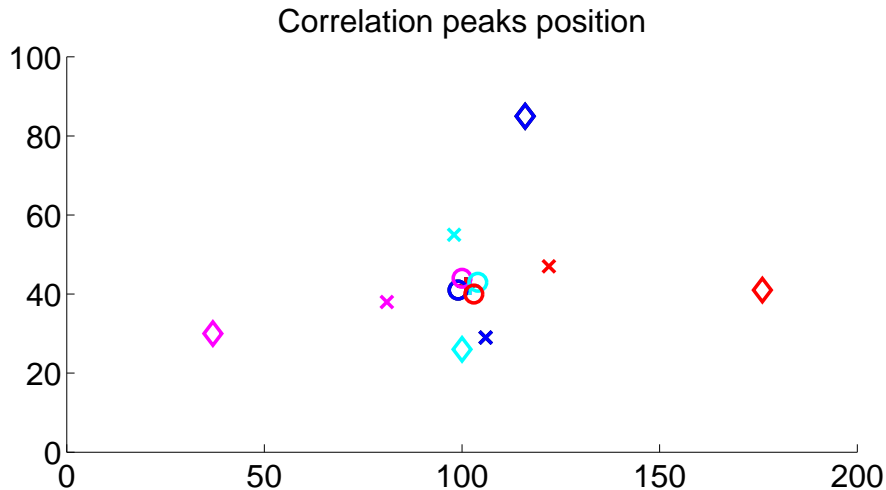


Figure 4.18: Specimen M1 correlation maxima position.
 Marker legend: + *bulge001*, ○ *bulge002*, ◇ *drill5mm001*, × *drill5mm002*.
 Color legend: blue: 0°, magenta: 90° cyan: 180° red: 270° clockwise.

Finally, it worth noting that, the response programmatically figured out by the algorithm, is visually evident from the bar diagram in Figure 4.2, which nicely shows the large gap of the correlation peak values. In particular, one may notice that the peaks of the two bulge template samples are quite nicely matching the same position, with an absolute error of 1 mm for some template orientation.

Specimen M2

A second wide acquisition has been performed on the 5 mm hole drilled plate depicted in Figure 4.8. The result of the specimen acquisition, is reported as reflectivity map reconstructed image in Figure 4.19.

Also in this case, the defect is clearly visible the central portion of the image, where the gradient highlights the decreasing value of pixels close to the hole. Moreover it is verified that the scale range is about the same order of magnitude compared to the one provided by that defect template.

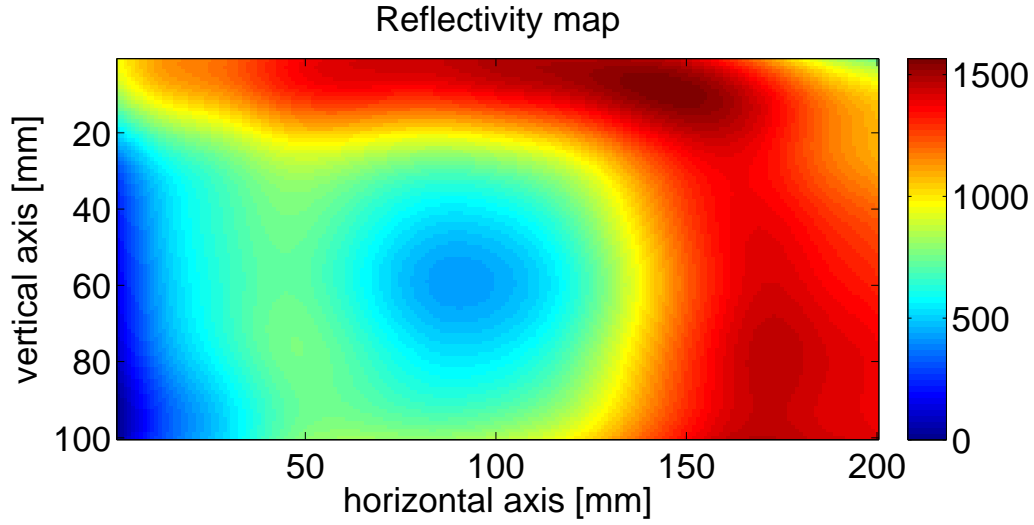


Figure 4.19: Specimen M2 reconstructed image ($\theta_x = \theta_y = 10^\circ$).

As opposed to the previous case, which has been used to introduce the algorithm full outcomes, from now on the specimen report is less detailed. In fact, the correlation maps are not herein reported, since the algorithm outcomes only depends on peaks values in Table 4.2.

Table 4.2: Specimen M2 - templates correlation peaks.

Template	0 degree		90 degree		180 degree		270 degree	
	max	coord	max	coord	max	coord	max	coord
<i>bulge001</i>	0.64	175,74	0.63	175,74	0.66	175,73	0.65	175,74
<i>bulge002</i>	0.75	174,74	0.61	45,70	0.57	50,69	0.68	175,73
<i>drill5mm001</i>	0.94	94,56	0.90	84,67	0.95	99,73	0.90	119,62
<i>drill5mm002</i>	0.57	82,75	0.91	166,75	0.65	119,26	0.85	55,55

Since it is visible in Figure 4.9 that the hole templates have a privileged direction (it is squeezed in the vertical direction), the templates matched only at 0 and 90 degrees of samples orientation. In fact, taking the means for each templates and any orientation, only hole sample figured out to rise the defect presence alarm at 90 degree (90.5%) and 270 degree (87.5%) overcoming the 85% threshold.

To sum up, it worth observing the bar diagram in Table 4.2, from which

is clear the gap between the hole matching.

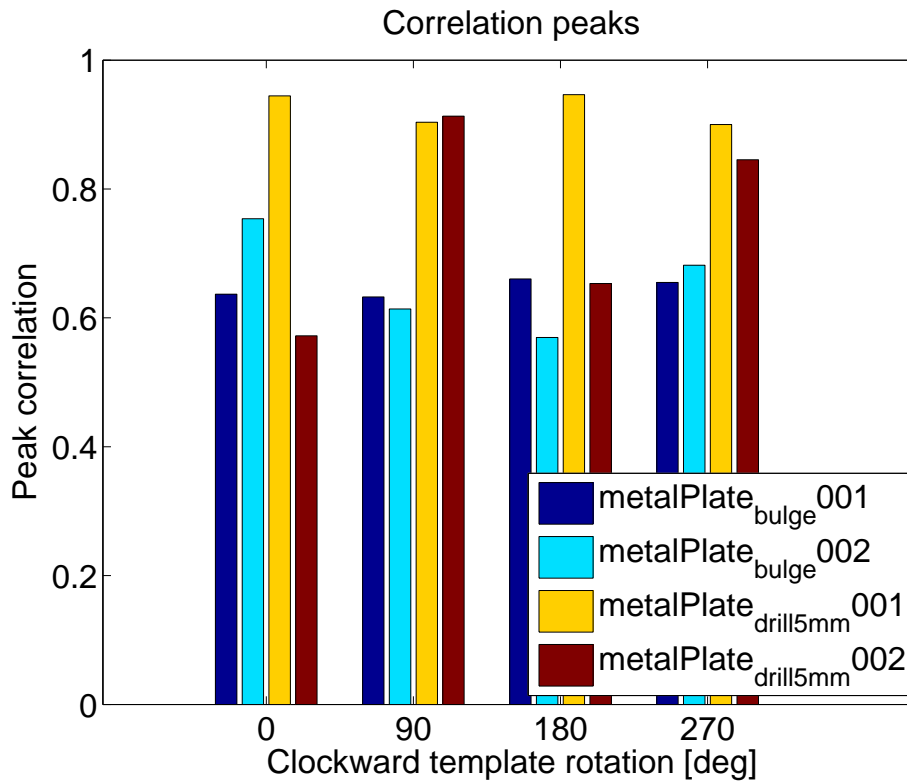


Figure 4.20: Specimen M2 correlation maxima.

4.4.2 Composite plate

Since a single defect kind has been scanned, only one composite full-plate acquisition has been performed to check the defect matching. The report of plate specimen named *Specimen C1* is reported below.

Specimen C1

The composite plate *Specimen C1* has a central 5 mm drilled hole. The generated reflectivity map is reported in Figure 4.21. Even though slightly not centered, the image of the specimen clearly shows the effect of EM field deviation due to the hole presence. It is also quite straightforward that the

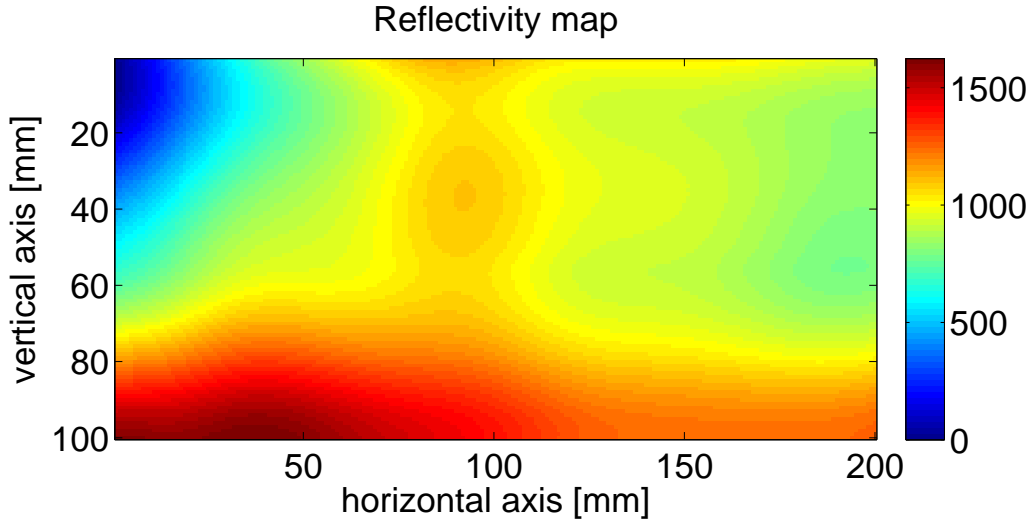


Figure 4.21: Specimen C1 reconstructed image ($\theta_x = \theta_y = 10^\circ$).

overall plate reflectivity has been modified by the presence of the defect, since the pixels range is limited below to 1600. Furthermore, the defect ROI appears to be quite small in magnitude, about of the same order of the one shown by the drilled hole template.

If we consider the software automatic response, Table 4.3 is filled with the correlation maxima found during template samples matching. It is easy to

Table 4.3: Specimen C1 - templates correlation peaks.

Template	0 degree		90 degree		180 degree		270 degree	
	max	coord	max	coord	max	coord	max	coord
<i>drill5mm001A_{crop}</i>	0.57	102,47	0.93	102,50	0.69	151,46	0.91	103,47
<i>drill5mm003A_{crop}</i>	0.57	150,49	0.88	104,50	0.69	150,43	0.89	101,48

notice that the threshold of 85% is overcome by both the defect samples, but only at two orientations, namely 90 and 270 degrees, with a mean value of about 90%. Moreover the position of the maximum for each of the matching templates is close to (103,50). Although the revolution geometry nature of the defect suggests it could be identified disregarding its orientation, this is not true in practical application. Nonetheless, the asymmetric reflectivity of the drilled hole plate was already accessed for the metal specimen. Thus, also

for the composite coupon, the EM field seems to have a similar privileged direction. Finally, a bar diagram is presented in Figure 4.22 to report the template matching for this composite specimen.

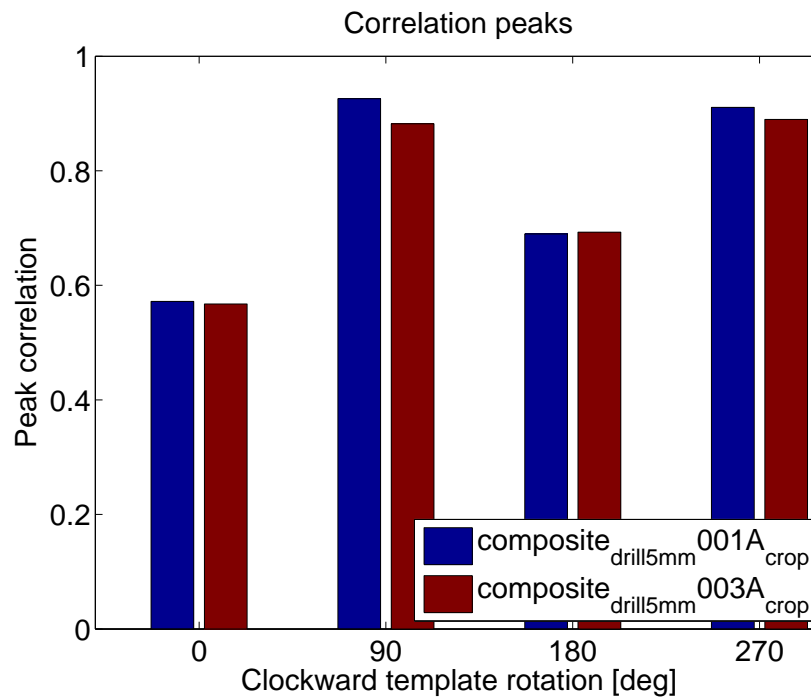


Figure 4.22: Specimen C1 correlation maxima.

Chapter 5

Conclusions

5.1 Shortcomings

Based on the NDIs classification provided in Section 1.2, a similar brief overview of the developed system is presented. It worth nothing that, although a typical SAR application involves large array of antennas to simultaneously observe a scene from multiple Point of Views (POVs), a different approach has been implemented in this thesis. Having a single radar device - moreover a bistatic one - required a virtual SAR to be programmatically built.

This consist in a step-by-step motion of the radar device, whose responses are collected into an observable matrix. Hence, the matrix is used as the response of a single-shot radar acquisition by means of antennas array, being aware of the time-dependent disturbance sources that may occur in a multiple time observation.

5.1.1 Method overview

The developed NDI system based on Novelda NVA6201 radar device exploits the illumination of the specimen with a UWB radar beam and the collection of the backscattered waveform. The EM field induced by the specimen, and thus its backscattering behavior, provides significant informations

on the state of the coupon itself. According to [15], the effect of a lossy medium drives the power of the EM signal to decay exponentially through the thickness of the sample, following the law

$$d_p \cong \sqrt{\frac{2}{2\pi f \mu \sigma}} \quad (5.1)$$

where f is the operating frequency, μ the magnetic permeability of the composite material assumed to be almost equal to the free space one (μ_o), and σ the electrical conductivity of the material. Since the employed waveform frequencies, from 5.65 to 7.95 GHz¹, do not allow any appreciable material penetration, thus this should be classified as a surface NDI. Although, the same study is capable to explain the EM response of the carbon fibers composite material, which are basically nonmagnetic, to the RF-based NDI, such as the one we are dealing with. In fact, the anisotropic behavior of the composites is induced by the conductive properties of the carbon fibers which react to the external EM stimulation by circular current loops along the contact points of the filaments. Hence, in case of flaws, delaminations or fibers cracking, the EM response of the material is different from the healthy one.

Technique

The procedure is performed by a step-by-step waveform acquisition, filling each cell of an imaginary grid to have a complete set of observation from several POVs. The combination of informations provided by this set of multiple observations is able to provide the reconstruction of the scene EM reflectivity map forming an image. Comparing this latter to a pre-compiled defects database, the algorithm generates statistical maps indicating the likelihood of each template occurrence on the specimen. In other words, it is not only able to provide an *image* of the specimen, intended as an EM reflectivity

¹Being $f_c = 6.8$ GHz and $W = 2.3$ GHz, the lower frequency and the upper one are, respectively, $f_l = f_c - \frac{W}{2}$ whilst $f_u = f_c + \frac{W}{2}$.

map, but also to know if a particular spot on the coupon is so similar to a specific template that we may reasonably assumed that kind of defect is present in that specific spot, and in which direction it is oriented with respect to the acquired template.

Overview

- This method is very cheap.
- It is not risky for operator health, since low emitted power is employed.
- It is applicable to any electrical conductive or EM reflective material with simple geometry (up to now only to completely flat specimen), although the handling of complex geometry is possible.
- It is only able to detect surface flaws (although in principle the specimen inner layers observation is possible using lower frequencies).
- It is recommended for end-of-line testing, due to its capability of similar defect recognition, may highlights industrial machine pathological tailoring defects.
- The method is automatic from acquisition to processing and results interpretation, even though a proper trained operator is necessary for specimen positioning and system calibration².

Summary

As we did for all of the NDIs presented in Chapter 1, also for UWB-SAR method design during this thesis we provide a short summary in Table 5.1.

Compared to other NDI methods, the UWB-SAR imaging has several important strength points. In fact, the response is not simply if a defect is present or not, but in principle it is able also to determine its shape by image reconstruction and its particular kind if it has been already inserted in the database. Moreover the method is quite flexible, and can be applied to a

²This could be avoided by introducing some system enhancement proposed in Section 5.2

Table 5.1: UWB-SAR NDI summary.

Materials	EM reflective, or electrical conductive.
Detectable defects	Surface damages.
Advantages	Cheap, contactless.
Disadvantages	Flat surface required.
Penetrating element	EM field.
Revelator element	UWB radar.
Pricing	Very low.

large variety of EM reflective or electrical conductive materials. The simple system let the price be very low, as well as the personnel health risks and the power consumption.

5.2 Future developments

Although the objective of this work to create a brand new NDI system employing a UWB-SAR system has been achieved, some important considerations could be done. Looking at the results with a critical sensibility could be very useful to suggest some improvements that could be implemented in some future works. The enhancements proposed regards:

1. the radar device
 - 1.a reliability;
 - 1.b stability and accuracy;
 - 1.c tuning of the centre frequency to penetrate the material and provide a sort of CT;
2. the motion device
 - 2.a provide multiple points laser DMS;
 - 2.b provide automatic centring system;
 - 2.c upgrade the stepper motors with faster and more precise ones;

2.d provide a closed loop control system, using a feedback on actual position (e.g. employs encoders, etc. . .).

Let us start from point 1 reporting the improvements required for the radar. Despite in Novelda datasheet [19] very little is specified about the continuous working condition, it has been a real issue. In fact, two following acquisitions were done consequently without resetting the device, but sometimes the peripheral PC port received data from the radar, which turned out to be nothing but noise. On the other hand, an higher clock stability and accuracy could be obtained by an higher price category radar. Concerning the last point about the radar device, it refers to the physical principle of the system. As very high central frequency (6.8 GHz) has been employed during the test campaign, the largest part of the specimen incident radiation was reflected. Otherwise, substantially decreasing the central frequency may provide (for non-metallic material which need to be experimentally tested) some material penetration capability. This involves that a part of the radiation will be reflected by lowers layers of the material, whose informations could be extrapolated from the return signal. In principle, looking at different *depth*, obviously compensating for diffraction effects and decreasing of wavespeed in the material, the images of inner layers of the specimen should be visible although in a less clear way due to material attenuation.

Passing to the motion device, the first enhancement to be done regards the distance to the specimen. Although some kinds of bars could be used to set it to a precise distance to the coupon, it should be preferred a contactless system as for instance a laser DMS. Despite one of this devices has been used during the thesis, it would be necessary to provide those measurements at some different points at the same time to be sure a precise alignment is obtained. Thus the suggestion is to implement some (eventually low cost) multiple devices placed at the opposite corners of the motion device, with accuracy in the order at least of the millimeter (tenth of millimeter is suggested). Furthermore a pointing system to provide defect centering when scanning a template could be adopted as well, maybe exploiting some laser beam from

the DMS. Moreover substituting the stepper motors with new generation ones could mean save a lot of acquisition time (which is now a real issue, since a 300×200 mm scanning area, at 1 mm steps took more than 22 hours) as well as reduce the noise and eventually have more precise movements. Finally, both to provide a more industrial suitable device and to prevent motors issues, a feedback could be provided by means of rotative encoders to track the instantaneous position of the radar, and - also exploiting physical triggers - to provide a end-of-the-line block safety system.

Of course, what described above only regards possible improvements about the actually existing system, without any dramatic changes. On the other hand, the application of different kinds of SAR, such as a phased array antenna, would have much more beneficial effects. In the particular case of the phased array antennas, we would have a quasi-instantaneous acquisition, which may let to reduce the scanning time dramatically up to few seconds. Moreover no motion device would be necessary and recalling the first rule of mechanical engineers *What you don't use, it doesn't break*, it turns out to be quite a great deal. Sparing lots of mechanical components, the risk of failure dramatically drop. A phased array antenna is a set of antennas, which exploits some particular devices called *phase shifters* to change the phase of each single waveform and eventually obtain a beam oriented in a desired direction through the superposition of each waveform front, as shown in Figure 5.1. This would easily make the work now provided by the motion device, moving the radar beam instead of the radar itself. For a 2D application such the one herein described, this is quite a easy task, but in principle it would be possible also for non-planar surfaces.

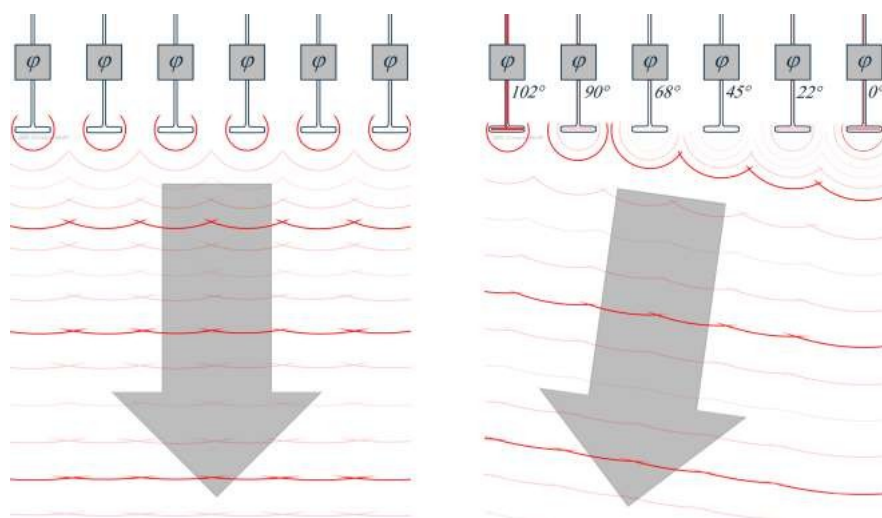


Figure 5.1: Phased array antenna working principle.

Bibliography

- [1] Alumeco.com. Ultrasonic testing of aluminum. <http://www.alumeco.com/Knowledge-and-Technique/Useful-Info--and-Tips/Ultrasonic-testing-of-Aluminium.aspx>.
- [2] ArmedForces.co.uk. http://www.armedforces.co.uk/companies/raq3f7406dced7e9#.VsRnE_nhCUk.
- [3] R. Bamler. Principles of synthetic aperture radar. *Surveys in Geophysics*, 21:147–157, 2000.
- [4] M. Chemie. Penetrant testing. <http://www.mr-chemie.de/en/products/penetrant-testing/description/>.
- [5] M. Cheney. A mathematical tutorial on synthetic aperture radar. *Society for Industrial and Applied Mathematics review*, 43(2):301–312, 2001.
- [6] S. P. Components. NDT Non-Destructive Testing and Inspection. <http://www.stellarprecision.com/quality/non-destructive-testing.html>.
- [7] Council of European Union. Council regulation (EU) no 2787/2009, 2009. Commission Decision of 21 April 2009 amending Decision 2007/131/EC on allowing the use of the radio spectrum for equipment using ultra-wideband technology in a harmonised manner in the Community (2009/343/EC).

- [8] Council of European Union. Council regulation (EU) no 522/2007, 2014. Commission Decision of 21 February 2007 on allowing the use of the radio spectrum for equipment using ultra-wideband technology in a harmonised manner in the Community (2007/131/EC).
- [9] Council of European Union. Council regulation (EU) no 7083/2014, 2014. Commission Implementing Decision of 7 October 2014 amending Decision 2007/131/EC on allowing the use of the radio spectrum for equipment using ultra-wideband technology in a harmonised manner in the Community (2014/702/EU).
- [10] M. Gamauf. Nondestructive testing and inspection. <http://aviationweek.com/mro-enterprise-software/nondestructive-testing-and-inspection>.
- [11] D. Gandhi. Non destructive tesing. <http://www.slideshare.net/DevangGandhi7/non-destructive-testing-51684910>.
- [12] S. Gubinelli. Studio di fattibilit  di applicazione di radar UWB per controlli non distruttivi. Ingegneria aerospaziale, Universita di Bologna, 2013.
- [13] S. Gubinelli, E. Paolini, A. Giorgietti, A. Rizzo, E. Troiani, and M. Chiani. An ultra-wideband radar approach to non-destructive testing. *IEEE International Conference on Ultra-WideBand (ICUWB)*, pages 303–308, 2013.
- [14] M. Jalilvand, T. Zwick, W. Wiesbeck, and E. Pancera. UWB synthetic aperture radar system for hemorrhagic head-stroke detection. *IEEE RadarCon*, pages 956–959, 2011.
- [15] Z. Li and Z. Meng. A review of the radio frequency non-destructive testing for carbon-fibre composites. *Measurement Science Review*, 16(2):68–76, 2016.

BIBLIOGRAPHY

- [16] P. E. Mix. *Introduction to Nondestructive Testing: a Training Guide*. Wiley Interscience, 2005.
- [17] Novelda. *Novelda 6.0 - 8.5 GHz Sinuous Antenna*, 0.1 edition, 2011.
- [18] Novelda. *Novelda Development Kit User Guide*, 3.0.5 edition, 2012.
- [19] Novelda. *NVA620x Preliminary Datasheet*, A edition, 2013.
- [20] E. Paolini. Radiocommunication and radar systems (for aerospace engineering). Classrom Notes, 2014.
- [21] J. Schijve. *Fatigue of Structures and Materials*. Springer, 2009.
- [22] A. Sullivan, R. Damarla, N. Geng, Y. Dong, and L. Carin. Ultrawide-band synthetic aperture radar for detection of unexploded ordnance: Modeling and measurements. *IEEE Transactions on Antennas and Propagation*, 48(9):1306–1315, September 2000.
- [23] The American Society for Nondestructive Testing. Introduction to non-destructive testing. <https://www.asnt.org/~media/Images/About/IntroductionToNDT/>.
- [24] US Federal Communication Commission. US Federal Communication Commission Title 47 Part 15 of the Commission Rules Applicable to UltraWideband Devices, 2014.
- [25] Vetorixgroup.com. Divisione aeronautica. <http://www.vetorixgroup.com/engineering/pages/aereonautica.htm>.
- [26] S. Wilkinson. Comparative testing of radiographic testing, ultrasonic testing and phased array advanced ultrasonic testing non destructive testing techniques in accordance with the aws d1.5 bridge welding code, 2014.
- [27] J. Worman. Magnetic particle examination. *National Board BULLETIN*, 2011. <http://www.nationalboard.org/index.aspx?pageID=164&ID=377>.

Acknowledgments

First of all I would like to thank professor Enrico Paolini who has followed me in each step of my thesis and turned out to be a great person on a human side as well as a very good teacher. Professor Enrico Troiani also deserves my gratitude for the structural technical background as well as professor Andrea Giorgetti for the contribution to the development of the system. Moreover, I would like to thank Drs Matteo Mazzotti, Anna Guerra and Nicol  Decarli for the radio communication background and Paolo Proli for the composite manufacturing.

Above all, thanks to my family, which always supported and spurred me to go on, in particular my girlfriend Alessia, my parents Paolo and Cosetta, my brother Davide and my sister Angelica.

Last but not least, I would like to thank those who shared with me the passion, the study (the joys and sometimes the failures) and a small piece of their lives: my university colleagues, those I knew from the Bachelor's, those I met at the Master. In particular, the ones of the *A5Unibo team* who I shared with the great adventure of the Bexus 18, among them Paolo and Marco who also helped me until the end of my thesis. And once again thanks to Danilo, Lucia and Giuseppe since, although we spend a great part of the Master's degree time at the opposite corners of Europe, they still are the greatest friends I knew right here, at the beginning of this trip which is going to end.